

# Poisson process factorization for mutational signature analysis with genomic covariates

Alessandro Zito<sup>1,2</sup>, Giovanni Parmigiani<sup>1,2</sup>, and Jeffrey W. Miller<sup>1</sup>

<sup>1</sup>*Department of Biostatistics, Harvard T.H. Chan School of Public Health, Boston, MA, U.S.A.*

<sup>2</sup>*Department of Data Science, Dana Farber Cancer Institute, Boston, MA, U.S.A.*

## Abstract

Mutational signatures are powerful summaries of the mutational processes altering the DNA of cancer cells and are increasingly relevant as biomarkers in personalized treatments. The widespread approach to mutational signature analysis consists of decomposing the matrix of mutation counts from a sample of patients via non-negative matrix factorization (NMF) algorithms. However, by working with aggregate counts, this procedure ignores the non-homogeneous patterns of occurrence of somatic mutations along the genome, as well as the tissue-specific characteristics that notoriously influence their rate of appearance. This gap is primarily due to a lack of adequate methodologies to leverage locus-specific covariates in the factorization directly. In this paper, we address these limitations by introducing a model based on Poisson point processes to infer mutational signatures and their activities as they vary across genomic regions. Using covariate-dependent factorized intensity functions, our Poisson process factorization (PPF) generalizes the baseline NMF model to include regression coefficients that capture the effect of commonly known genomic features on the mutation rates from each latent process. Furthermore, our method relies on sparsity-inducing hierarchical priors to automatically infer the number of active latent factors in the data, avoiding the need to fit multiple models for a range of plausible ranks. We present algorithms to obtain maximum a posteriori estimates and uncertainty quantification via Markov chain Monte Carlo. We test the method on simulated data and on real data from breast cancer, using covariates on alterations in chromosomal copies, histone modifications, cell replication timing, nucleosome positioning, and DNA methylation. Our results shed light on the joint effect that epigenetic marks have on the latent processes at high resolution.

Keywords: Cancer genomics; Latent factor models; Mutational signatures analysis; Non-negative matrix factorization; Poisson point processes.

# 1 INTRODUCTION

## 1.1 MOTIVATION

Cancer is associated with the progressive accumulation of mutations in the genome of the somatic cells of the body (Stratton et al., 2009). These mutations manifest in distinctive patterns called *mutational signatures*, which are latent vectors encoding the probability of various mutation types (Nik-Zainal et al., 2012, 2016; Alexandrov et al., 2013; Kucab et al., 2019). Each signature represents a specific biological process, such as failures in the DNA repair mechanisms, oxidative stress, or exposures to exogenous carcinogens like tobacco smoking or ultraviolet light. Crucially, their correct identification in patients has led to several improvements in precision therapies (Aguirre et al., 2018; Gulhan et al., 2019; Samur et al., 2020), making mutational signature analysis a recent milestone in cancer research (Alexandrov et al., 2020). Refer to Koh et al. (2021) for an overview, and to the *Catalogue of Somatic Mutations in Cancer* (COSMIC; Tate et al., 2018) for a curated collection of signatures and their etiology across multiple tumors and environmental agents.

Somatic mutations are identified by comparing genomes from cancer cells against those from healthy cells in the same tissue using next-generation sequencing technologies and variant calling algorithms (Benjamin et al., 2019). This process returns both the *mutation type*—for instance, a C>T single-base substitution (SBS)—and its *genomic coordinate*, that is, the position of the mutation within a chromosome. Subsequently, one applies dimensionality reduction methods, such as non-negative matrix factorization (Lee and Seung, 1999; Alexandrov et al., 2013) or the hierarchical Dirichlet process (Teh et al., 2006; Martínez-Ruiz et al., 2023), to the matrix of mutation counts obtained from patients with similar diagnoses. Then, the inferred signatures are compared with the COSMIC catalog to shed light on the underlying biological processes at play. Such a pipeline is advantageous in being agnostic to the specificity of the tumor under investigation, which has favored abundant development of methods and software to streamline inference, both for single-study (Fischer et al., 2013; Rosales et al., 2016; Kim et al., 2016; Blokzijl et al., 2018; Wang et al., 2020; Li et al., 2020; Islam et al., 2022; Pandey et al., 2022; Díaz-Gay et al., 2023; Liu et al., 2023; Drummond et al., 2023; Jin et al., 2024; Pancotti et al., 2024; Landy et al., 2025) and multi-study settings (Grabski et al., 2025; Hansen et al., 2025).

However, the vast majority of the aforementioned tools operate at an *aggregate scale* and learn mutational signatures by considering only the total number of mutations detected along the genome of each patient. This comes with two fundamental limitations. First, modeling aggregate counts implicitly entails a constant rate of mutation across genomic regions, and such a simplifying assumption is rarely met in practice. This is evident from Figure 1(a), which displays the number of single-base substitutions (SBS) in one-megabase-wide bins from 113 breast cancer patients. While many regions feature around 200 mutations, many others show either heavily inflated or depleted counts. Second, the *topography* of the genome—namely the collection of epigenetic modifications determining its spatial and functional arrangements—is ignored in the factorization, thus hiding the important regulatory mechanisms that impact the mutational landscape in cancer. Indeed, it has been well observed that epigenetic marks deeply influence mutation occurrences at various resolutions (Makova and Hardison, 2015; Supek and Lehner, 2019). For instance, histone modification H3K9me3 can account for nearly 40% of the variation in mutation rate at the megabase scale in many tumors (Schuster-Böckler and Lehner, 2012), while early replicating euchromatin is less prone to mutations due to preferential mismatch repair functions (Supek and Lehner, 2015; Li et al., 2013). Moreover, tumors like breast cancer often feature

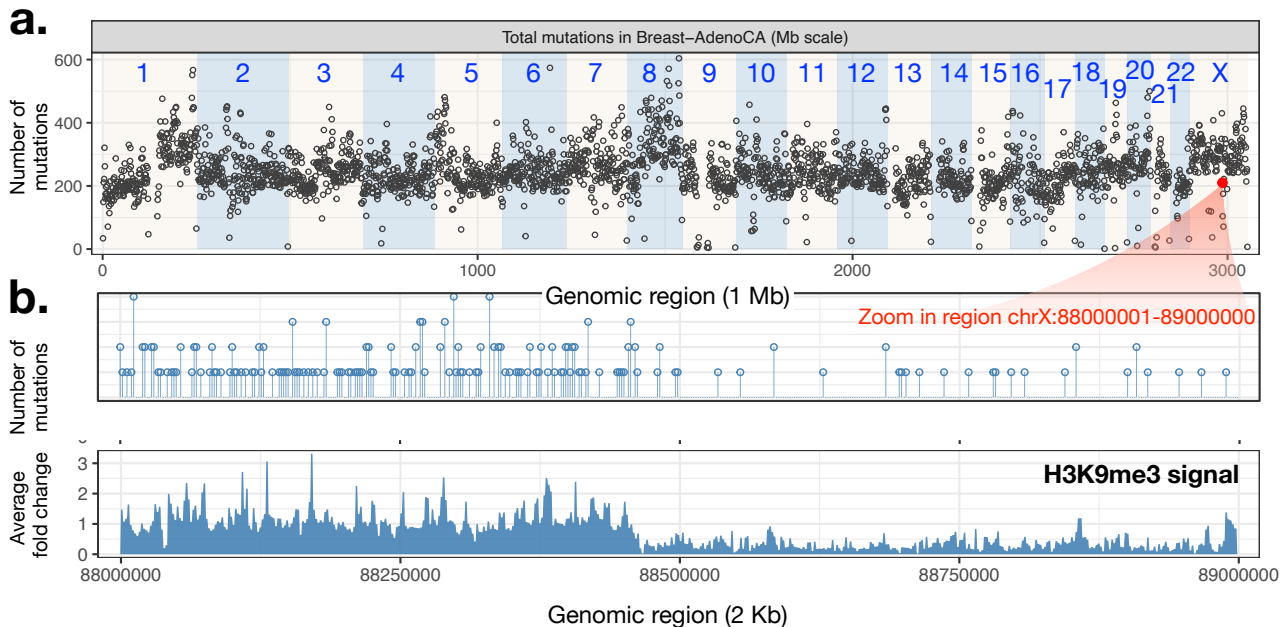


Figure 1: (a) Number of single-base substitutions one-megabase bins in the ICGC **Breast-AdenoCA** data. Alternating colored bands and numbers indicate chromosomes. (b) Top: number of mutations 2 kilobase bins for region chrX:88,000,001-89,000,000, highlighted by the red point. Bottom: average fold change signal in the same bins for histone modification H3K9me3, in breast epithelium tissue (ENCODE file `ENCF764JHZ.bigwig`).

alterations in the number of chromosomal copies, which lead to catastrophic dysregulations of cell functions and variation in mutation occurrences (Shahrouzi et al., 2024). Figure 1(b) shows an example where the number of mutations falling into 2-kilobase bins correlates with the signal from H3K9me3, calculated as average fold-change with respect to a baseline value from a ChIP-seq assay.

The goal of this work is to introduce a model where mutational signatures and their activities are inferred from the local genomic characteristics associated with each detected mutation. We provide details on the covariates used in this paper in the next section. Then, in Section 1.3, we describe current tools in the literature to assess the relationship between mutational signatures and these covariates. Our improvements and methodological contributions are discussed in Section 1.4.

## 1.2 OVERVIEW OF GENOMIC COVARIATES

Cellular activity is regulated by the interaction between the *genome* and the *epigenome*, where *epi-* is a Greek prefix meaning “above”. The first is fairly homogeneous across cells, while the second encompasses the cell-specific chemical modifications that control DNA functions, including chromatin conformation, regulation of transcriptional activities of genes, and repair mechanisms (Jaenisch and Bird, 2003). To measure these activities at various genomic locations, an abundance of data has been collected from various assays and experiments over the last decade, with the Encyclopedia of DNA Elements (ENCODE; Abascal et al., 2020) being the largest publicly accessible collections in the field. Table 1 describes the covariates we use in this paper and summarizes their known effect on the aggregate mutation rate. For a complete account of the impact of chromatin conformation on mutations at the various scales, see Makova and Hardison (2015) and Supek and Lehner (2019).

Table 1: Description of genomic and epigenetic covariates used in the application in Section 5. The column ASSAY indicates the assay used to obtain the covariate. MNase-seq: Micrococcal Nuclease; TF ChIP-seq: Chromatin immunoprecipitation for transcription factors; Histone ChIP-seq: Chromatin immunoprecipitation for histone modifications; Repli-seq: Replication timing; WGBS: Whole Genome Bisulfite Sequencing. Column MUTATIONS describes the known associations between the covariate and the mutation rate in cancer (not necessarily breast). Symbol  $\nearrow$  and  $\searrow$  indicate a positive and a negative effect, respectively. REFERENCE indicates the work where the association is mentioned.

| COVARIATE            | ASSAY            | DESCRIPTION AND ROLE  | MUTATIONS                                | REFERENCE                          |
|----------------------|------------------|---|--|------------------------------------|
| Nucleosome occupancy | MNase-seq        | Degree to which DNA is wrapped around nucleosomes; higher values indicate packed chromatin.           | Periodic patterns                        | Pich et al. (2018)                 |
| H3K27ac              | Histone ChIP-seq | Marker of active enhancers and promoters; associated with gene activation.                            | $\nearrow$                               | Schuster-Böckler and Lehner (2012) |
| H3K4me1              | Histone ChIP-seq | Marks poised and active enhancers; enriched at regulatory elements.                                   | $\searrow$                               | Hodgkinson et al. (2012)           |
| H3K4me3              | Histone ChIP-seq | Marks active promoters; associated with transcription initiation.                                     | $\searrow$                               | Hodgkinson et al. (2012)           |
| H3K9me3              | Histone ChIP-seq | Marker of constitutive heterochromatin; gene silencing/repression.                                    | $\nearrow$                               | Schuster-Böckler and Lehner (2012) |
| H3K27me3             | Histone ChIP-seq | Repressive mark, associated with Polycomb-mediated gene silencing.                                    | $\nearrow$                               | Schuster-Böckler and Lehner (2012) |
| H3K36me3             | Histone ChIP-seq | Marker of transcriptional elongation within gene bodies.  | $\searrow$                               | Li et al. (2013)                   |
| CTCF                 | TF ChIP-seq      | Insulator protein, key architectural TF regulating chromatin looping and gene expression.             | $\nearrow$                               | Katainen et al. (2015)             |
| Replication timing   | Repli-seq        | Timing of DNA replication during S-phase of a cell; reflects chromatin state and genome organization. | $\nearrow$ (later)<br>$\searrow$ (early) | Supek and Lehner (2015)            |
| Methylation          | WGBS             | Level of DNA methylation; regulates gene expression and silencing.                                    | $\nearrow$ at CpGs                       | Bird (1980)                        |
| GC content           | —                | Proportion of G and C nucleotides a region; influences DNA stability and nucleosome positioning.      | $\searrow$                               | Makova and Hardison (2015)         |

The core building block of the spatial conformation of the genome is the *nucleosome*, a segment of 147 DNA base pairs wrapped around four pairs of *histone* proteins called H2A, H2B, H3, and H4. Nucleosomes are separated by 60-80 base pairs, forming “linker DNA”. Their relative position determines the type of chromatin in a given region and, subsequently, its accessibility. When nucleosomes are closely packed with each other—forming the *heterochromatin*—transcription is usually suppressed, and damages to DNA are harder to repair. In such regions, a higher frequency of somatic mutations has been observed in many cancers (Schuster-Böckler and Lehner, 2012). On the contrary, looser regions—generating the *euchromatin*—exhibit fewer mutations (Polak et al., 2015). Current analyses suggest that the signal from nucleosome occupancy exhibits periodic patterns around DNA mutations, with behaviors varying depending on the mutational signatures to which these mutations are attributed (Otlu et al., 2023).

The relative position and density of nucleosomes are influenced by the *histone modifications*, which are chemical reactions happening in the protein residues of the histones. For instance, mark H3K36me3 indicates 3 molecules of methyl group (me3) bound to the 36th lysine (K) in the amino acid residue of histone H3, causing elongations and favoring accessibility (Li et al., 2013). On the contrary, H3K9ac is short for one molecule of acetyl group (ac) in the 9th lysine and is associated with gene activation. Depending on the modification at play, genomic regions can have high or low mutational burden; see Table 1. Moreover, genomic architecture is also shaped by sequence-specific DNA-binding proteins such as the transcription factor CTCF, which acts as an insulator and helps organize chromatin loops and domains. Previous analyses of cancer genomes showed

increased mutation rates in CTCF binding sites (Katainen et al., 2015). Both CTCF and histone modifications are measured via chromatin immunoprecipitation (ChIP-seq assay).

Another important genomic regulator is the timing of DNA replication during the S-phase of the cell cycle, known as *replication timing* (Thurman et al., 2007). Early-replicating regions are usually populated with genes and are highly accessible, while late-replicating regions tend to be heterochromatic (Stamatoyannopoulos et al., 2009). Replication timing is estimated via Repli-seq (Hansen et al., 2010), which labels and sequences DNA synthesized at different stages of S-phase; timing values are computed by smoothing a weighted average of the proportion of early and late replicating cells in 1kb windows. By construction, low values of replication timing indicate that the region tends to replicate *later*, while high values denote regions that replicate *early*. Mutational signatures are largely enriched in late-replicating regions (Otlu et al., 2023).

Finally, DNA *methylation* is a key mutation driver (Bird, 1980). Primarily, methylation binds a methyl group to CpG loci to form 5-methylcytosine, leading to spontaneous deamination and C>T substitutions (Nishiyama and Nakanishi, 2021). In COSMIC, this behavior is responsible for the ubiquitous signature SBS1, which also correlates with patient age (Alexandrov et al., 2015). Moreover, the overall fraction of the number of G and C nucleotides in a given genomic segment—referred to as GC content—is a strong predictor of the degree of transcription, gene expression, and replication timing in that segment. The total GC content in the hg19 genome is around 40%, but regions may peak at 80% at the kilobase scale.

### 1.3 PREVIOUS WORK ON EPIGENETIC MARKS AND MUTATIONAL SIGNATURES

There are a few methods that investigate the regional variations in mutational signatures and their relationship with topographic features, and each targets a specific goal. In this section, we briefly describe them and highlight their potential limitations.

The first example in the literature is EMu (Fischer et al., 2013), which infers signatures and their activities by dividing the genome into megabase regions, fitting a separate NMF for each bin. Meanwhile, GenomeTrackSig (Timmons et al., 2022) detects regional variation in signature activities by partitioning the genome into bins, and then performing a changepoint detection analysis. Each bin is recommended to have at least 100 mutations. Neither method incorporates epigenetic covariates into the model. A step in this direction is taken by TensorSignatures (Vöhringer et al., 2021), which applies Tucker-like factorizations to a tensor of mutations differentiated by mutually exclusive chromatin states (Ernst and Kellis, 2017). While the model also considers replication strands, it cannot leverage continuous covariates in the factorization. Moreover, benchmarking analyses indicated sub-optimal performance (Islam et al., 2022).

Recently, a compendium of the topographical features related to each signature has been assembled by Otlu et al. (2023) and subsequently by Otlu and Alexandrov (2025) via the SigProfilerTopography software. Their goal is to test for enrichments or depletions of the detected mutations for given topographic marks by comparing the real data against simulated mutations, placed uniformly at random along the genome. This is, however, a post-hoc analysis tool: mutations in patients are pre-assigned to a specified set of signatures and activities, and values for each covariate are then averaged by position and patient using a 2kb window centered around the mutations. Hence, the method is useful to test the aggregate effects of individual topographic marks, but not their *joint* effect on the mutation rate.

Additional post-hoc analyses and tools for regional variations in mutational signatures and their relationships with genomic covariates are described in [Blokzijl et al. \(2018\)](#); [Lee et al. \(2018, 2022\)](#) and [Schmalohr \(2025\)](#). In all cases, these approaches always consider a pre-determined set of signatures and exposures in the inferential step. To our knowledge, no method in the literature currently allows for estimation of the latent structure while also testing the impact of the effect of genomic covariates at a given resolution at the same time.

## 1.4 OUR CONTRIBUTIONS

The goal of this work is to introduce a novel approach to mutational signature analysis where signatures and their exposures can be inferred by leveraging the local characteristics described in Table 1. Specifically, we model mutation occurrences as realizations from a collection of non-homogeneous Poisson point processes ([Kingman, 1993](#); [Daley and Vere-Jones, 2003](#)) acting simultaneously along the genome. The intensity function of each process has itself a parts-based latent representation where mutational signatures are shared across all genomic regions, while their activities depend on both the selected covariates and the number of chromosomal copies in each region for each patient. Local deviations in the mutation rate are captured in a multiplicative manner using a log-linear model in which signatures each have their own set of regression coefficients. Hence, our framework is highly interpretable thanks to its connection to Poisson generalized linear models ([Truccolo et al., 2005](#)). Moreover, it differs from previous approaches for point processes with a factorized intensity function ([Miller et al., 2014](#); [Lloyd et al., 2016](#); [Hosseini et al., 2020](#)), which are primarily designed to capture either spatial or temporal autoregressive trends in the data rather than covariate-driven effects.

We show how our Poisson process factorization (PPF) model has two important advantages when applied to mutational signature analysis. First, it provides a position-specific probability that a certain mutation type in a patient is attributed to a signature. In contrast, the classic Poisson NMF setting assigns a constant signature attribution probability to the same patient-mutation type pair, irrespective of its genomic location within a chromosome. Second, the regression coefficients flexibly capture enrichments or depletions in the mutational burden associated with the covariates for a specific latent process. Consequently, our model returns interpretable latent factors that are directly driven by known biological processes, such as methylation or H3K36me3-based repair mechanisms, yielding novel insights into the tumor under investigation.

On top of the aforementioned properties, the model leverages Bayesian hierarchical compressive hyperpriors ([Zito and Miller, 2024](#)) to perform automatic selection for the number of active signatures in the data. As we demonstrate in our empirical analyses, this bypasses the need to fit multiple models to determine the appropriate rank of the factorization, since the activities of redundant signatures are naturally shrunk to negligible values under such priors. This behavior is similar in spirit to overfitted mixture models ([Rousseau and Mengersen, 2011](#)) and avoids computationally intensive elicitation steps. We show how model parameters can be estimated using majorization-minimization algorithms ([Lee and Seung, 2000](#)) paired with a Fisher scoring method to obtain *maximum a posteriori* solutions. In addition, we present a Markov chain Monte Carlo algorithm that enables uncertainty quantification on the model parameters. We test our method on simulated data and on the real data from breast cancer in Figure 1, using the covariates described in Table 1.

The remainder of the article is structured as follows. Section 2 provides background on NMF in the context of mutational signatures, then introduces the Poisson process factorization model and the prior structure. Section 3

presents algorithms for posterior inference. Section 4 conducts a simulation study, and Section 5 applies the method to breast cancer data. Concluding remarks and future directions are discussed in Section 6.

## 2 MODEL

### 2.1 BASELINE POISSON NMF FOR MUTATIONAL SIGNATURE ANALYSIS

We begin by providing background on mutational signature analysis and non-negative matrix factorization. Our primary focus is on single-base substitutions (SBS), which are the most frequent DNA mutations in cancer (Alexandrov et al., 2020). Recall that DNA has a double-stranded structure where nucleotide A always binds with T, and C always binds with G. Due to this symmetry, only six possible substitutions can happen at any genomic position: C>A, C>T, C>G, T>A, T>C, T>G, where the nomenclature C>A denotes a mutation from the pair C:G into the pair A:T. The specific properties of the substitution have been observed to vary depending on the genomic context (Nik-Zainal et al., 2012). Thus, it is common practice to categorize substitutions by considering the adjacent nucleotides on each side of the mutation as well, leading to a total of  $I = 4 \times 6 \times 4 = 96$  possible *mutational channels* or *motifs*. For instance, T[C>A]G indicates a C>A mutation where T and G are the base pairs flanking C in a healthy genome.

Let  $N_{ij} \in \mathbb{N} = \{0, 1, 2, \dots\}$  indicate the number of mutations from patient  $j = 1, \dots, J$  in channel  $i = 1, \dots, I$ , and let  $N \in \mathbb{N}^{I \times J}$  denote the matrix with entries  $N_{ij}$ . Mutational signature analysis applies non-negative matrix factorization (NMF; Lee and Seung, 1999) to approximate  $N$  by the product  $R\Theta$ , where  $R \in \mathbb{R}_+^{I \times K}$  is the *mutational signature* matrix, and  $\Theta \in \mathbb{R}_+^{K \times J}$  is the *exposure* or *activity* matrix. Here,  $K \geq 1$  is the rank of the factorization and indicates the number of active processes mutating the genomes. Both matrices are obtained by minimizing a desired loss function, such as the squared Euclidean distance or the Kullback–Leibler divergence. Refer to the monograph of Gillis (2020) for an extensive overview of NMF.

From a modeling perspective, optimizing the Kullback–Leibler divergence is equivalent to letting

$$N_{ij} \sim \text{Poisson}\left(\sum_{k=1}^K r_{ik}\theta_{kj}\right) \quad (1)$$

independently for each pair  $i$  and  $j$ , where  $\text{Poisson}(\lambda)$  indicates the Poisson distribution with mean  $\lambda$ . Here,  $r_k = (r_{1k}, \dots, r_{Ik})$  and  $\theta_k = (\theta_{k1}, \dots, \theta_{kJ})$  are the  $k$ th column of  $R$  and the  $k$ th row of  $\Theta$ , respectively. When one imposes  $\sum_{i=1}^I r_{ik} = 1$ , the quantity  $r_{ik}$  is interpreted as the probability of observing a mutation of channel  $i$  from signature  $k$ , and  $\theta_{kj}$  represents its activity in patient  $j$ . See Rosales et al. (2016); Zhou and Carin (2015); Zito and Miller (2024) for more details on model-based approaches to NMF in count data.

Equation (1) specifies a model for the total number of mutations detected in each patient. However, information on the position of each mutation beyond the trinucleotide context is ignored. As we illustrate in Section 5, many regulatory elements along the genome influence mutation occurrences in tumors, but linking these covariates to Equation (1) is not straightforward. In the following sections, we present a model based on stochastic processes where such a link is possible.

## 2.2 POISSON PROCESS FACTORIZATION

Our main strategy consists of modeling the occurrences of mutations of type  $i$  in patient  $j$  as realizations from an inhomogeneous Poisson point process. Let  $([0, T], \mathcal{T})$  be a measurable space where  $T \geq 0$  represents the length of a hypothetical genome, and let  $A \in \mathcal{T}$  be a measurable set representing a given genomic region. Call  $N_{ij}(A)$  the number of mutation occurrences detected in  $A$ . Then, given a *intensity function*  $\lambda_{ij} : [0, T] \rightarrow \mathbb{R}_+$ , a Poisson point process is a counting process according to which (i) the number of points falling in  $A$  follows  $N_{ij}(A) \sim \text{Poisson} \left\{ \int_A \lambda_{ij}(t) dt \right\}$ , and (ii) for any other region  $A' \in \mathcal{T}$  so that  $A \cap A' = \emptyset$ ,  $N_{ij}(A')$  and  $N_{ij}(A)$  are independent. Here, the intensity determines the average number of points in  $A$ , with  $\mathbb{E}\{N_{ij}(A)\} = \int_A \lambda_{ij}(t) dt$ . When  $\lambda_{ij}(t) = \lambda$  is constant over all  $t$ , the process is called *homogeneous* and  $\mathbb{E}\{N_{ij}(A)\} = \lambda_{ij}|A|$ ; otherwise the process is *inhomogeneous*. See [Kingman \(1993\)](#) for a complete overview.

Suppose now that for each pair  $i, j$ , we observe  $N_{ij}$  mutations at positions  $t_1, \dots, t_{N_{ij}}$ , with  $t_n \in [0, T]$  for each  $n = 1, \dots, N_{ij}$ . For example, in our application, we may detect motif  $i = \text{G}[\text{T} > \text{C}]\text{C}$  at position  $t = \text{chr1}:233,224,563$  in chromosome 1, and  $T \approx 3$  billion base-pairs in total, divided across 23 chromosomes in female patients; see [Figure 1](#). Then, by construction, the likelihood function for the random positions  $t_n$  at each  $i, j$  is written as

$$\mathcal{L}(N_{ij}; t_1, \dots, t_{N_{ij}}) = \exp \left\{ - \int_0^T \lambda_{ij}(t) dt \right\} \prod_{n=1}^{N_{ij}} \lambda_{ij}(t_n). \quad (2)$$

Refer to Chapter 2 of [Daley and Vere-Jones \(2003\)](#) for a detailed derivation. Further assuming all realizations from pairs  $i, j$  as independent, the likelihood is then  $\mathcal{L}(\{N_{ij}; t_1, \dots, t_{N_{ij}}\}_{ij}) = \prod_{ij} \mathcal{L}(N_{ij}; t_1, \dots, t_{N_{ij}})$ .

The specification arising from Equation (2) is extremely flexible, and has been used in a broad variety of applications for spatiotemporal data ([Diggle, 2013](#); [Kang et al., 2025](#)). The crucial modeling step is the choice of the functional form of the intensity  $\lambda_{ij}$ . Mirroring Equation (1), we define these functions as

$$\lambda_{ij}(t) = \sum_{k=1}^K r_{ik}(t) \vartheta_{kj}(t), \quad t \in [0, T], \quad (3)$$

for each channel  $i = 1, \dots, I$  and patient  $j = 1, \dots, J$ , where  $K \geq 1$  is again the rank of the factorization,  $r_{ik} : [0, T] \rightarrow [0, 1]$  and  $\sum_i r_{ik}(t) = 1$  for every  $t$  is the  $k$ th mutational signature and  $\vartheta_{kj} : [0, T] \rightarrow \mathbb{R}_+$  its location-varying *exposure function* for patient  $j$ . Hence,  $r_{ik}(t)$  and  $\vartheta_{kj}(t)$  represent the probability of channel  $i$  and the activity at patient  $j$  associated with the  $k$ th process at each locus  $t$ , respectively. We refer to the above equation as the *Poisson process factorization* model (PPF). As the following proposition shows, Equation (3) has an important connection to NMF.

**Proposition 1.** *Consider the collection of inhomogeneous Poisson processes  $N_{ij}(\cdot)$  with intensity function defined in Equation (3). If  $T = 1$ ,  $r_{ik}(t) = r_{ik}$ , and  $\vartheta_{kj}(t) = \theta_{kj}$  for all  $t \in [0, T)$  and all triplets  $i, j, k$ , then inference in Equation (1) and Equation (2) is equivalent.*

Hence, when the exposure and the signature functions are constant, one retrieves the baseline Poisson NMF problem. Notice also that the value  $T = 1$  is arbitrary, since  $\int_0^T r_{ik} \theta_{kj} dt = T r_{ik} \theta_{kj}$  and therefore any value can be absorbed in the constant  $\theta_{kj}$  through appropriate rescaling. As a result, Equation (3) is a generalization of NMF that allows additional flexibility when inferring the latent factors. For a related generalization that accounts for temporal recurrences in the context of user-item recommendations, see [Hosseini et al. \(2020\)](#).

The next result, which is a direct consequence of the superposition theorem (Kingman, 1993), shows that the model in Equations (2) and (3) admits a parts-based representation like NMF (Lee and Seung, 1999), allowing us to interpret the mutation rate as a sum of distinct mutational processes acting independently.

**Proposition 2.** *Let  $Y_{ij1}(\cdot), \dots, Y_{ijK}(\cdot)$  be a collection of  $K$  independent inhomogeneous Poisson processes, so that  $Y_{ijk}(\cdot)$  has intensity function  $\lambda_{ijk}(t) = r_{ik}(t)\vartheta_{kj}(t)$ , for every  $t \in [0, T)$ . Then,  $N_{ij}(\cdot) = \sum_{k=1}^K Y_{ijk}(\cdot)$  is a Poisson process with intensity function as in Equation (3).*

### 2.3 LOCALLY-VARYING ACTIVITIES

The fundamental property of Equation (3) is that it is fairly general, since both signatures and exposures depend on  $t$ . In this work, we assume signatures to be constant along the genome, namely

$$(r_{1k}(t), \dots, r_{Ik}(t)) = (r_{1k}, \dots, r_{Ik}), \quad t \in [0, T), \quad (4)$$

for all  $k$ . Hence, only the activities are allowed to vary with the genomic location. While richer specifications are possible, this allows us to interpret variations in the mutation rate as variations in the activity of specific signatures. Moreover, by pooling  $r_k$  along  $[0, T)$ , one can directly compare the inferred signatures against the reference signatures in COSMIC (Tate et al., 2018) and therefore understand the underlying biological processes at play more transparently; see further comments in Section 6.

We now present a model that leverages genomic covariates and patient-specific characteristics to infer the locally-varying exposures  $\vartheta_{1j}(t), \dots, \vartheta_{Kj}(t)$  over  $[0, T)$ . Suppose that one observes  $p$  known covariate functions  $x_\ell: [0, T) \rightarrow \mathbb{R}$  for  $\ell = 1, \dots, p$ , with  $x_\ell(t)$  denoting the value of covariate  $\ell$  at position  $t$ , and denote their vector representation by  $\mathbf{x}(t) = (x_1(t), \dots, x_p(t)) \in \mathbb{R}^p$ . Furthermore, let  $c_j: [0, T) \rightarrow \mathbb{R}_+$  be a non-negative function capturing the mutation opportunities for a given patient  $j$  at every location. For example, if  $t$  is a genomic coordinate, then  $\mathbf{x}(t)$  may be the intensity of the signal detected from several histone modifications—such as H3K36me3, H3K27ac, or H3K9me3 as in Figure 1—for that nucleotide position in a *reference epigenome*. Moreover,  $c_j(t)$  can represent the number of chromosomal copies detected in patient  $j$  at  $t$ . Then, we define the location-varying activities using a log-linear model where

$$\vartheta_{kj}(t) = \frac{1}{2} \theta_{kj} c_j(t) e^{\boldsymbol{\beta}_k^\top \mathbf{x}(t)}, \quad t \in [0, T), \quad (5)$$

in Equation (3), with  $\theta_{kj} \geq 0$  for each  $k, j$ , and  $\boldsymbol{\beta}_k = (\beta_{k1}, \dots, \beta_{kp}) \in \mathbb{R}^p$  for each  $k$ .

The parameters of the function in Equation (5) have the following interpretation. Similarly to Poisson NMF,  $\theta_{kj}$  is the baseline activity of mutational signature  $k$  in patient  $j$ . Meanwhile,  $\boldsymbol{\beta}_k$  is a vector of regression coefficients capturing the effect of variations in  $\mathbf{x}(t)$  on the mutation rate induced by signature  $k$  at position  $t$ . As is typical of log-linear models, the proposed effect is *multiplicative*: a one-unit increase of  $x_\ell(t)$  at  $t$  implies an  $e^{\beta_{k\ell}} - 1$  percentage increase in the intensity of the  $k$ th latent process. In particular,  $\boldsymbol{\beta}_1, \dots, \boldsymbol{\beta}_K$  are common to all patients since  $\mathbf{x}(t)$  is from a set of reference covariates. Meanwhile,  $c_j(t) \geq 0$  is a quantity that captures the propensity of a region to be mutated in patient  $j$ , irrespective of the signature. In our application,  $c_j(t) = 2$  when there are two copies of the chromosome at position  $t$  in patient  $j$ . Since this is the default in the cells of the human body and mutations can be detected in both copies of the chromosome, we further multiply everything

by one-half so that  $c_j(t)/2 = 1$  represents the normal condition. Thus, if a patient has four copies of a genomic region, we may expect the total number of detectable mutations for that region to double, keeping all other quantities fixed. Finally, if  $c_j(t) = 2$  and  $\beta_k = 0$  for all  $k$  or  $\mathbf{x}(t) = 0$  for all  $t$ , then we retrieve the baseline constant exposures  $\vartheta_{kj}(t) = \theta_{kj}$  described in Proposition 1.

Altogether, under our model, the expected number of mutations of type  $i$  in patient  $j$  in region  $A$  is

$$\mathbb{E}\{N_{ij}(A) \mid R, \Theta, B\} = \sum_{k=1}^K r_{ik} \theta_{kj} \int_A \frac{1}{2} c_j(t) e^{\beta_k^\top \mathbf{x}(t)} dt, \quad (6)$$

where  $R = (r_{ik}) \in \mathbb{R}^{I \times K}$ ,  $\Theta = (\theta_{kj}) \in \mathbb{R}^{K \times J}$  and  $B = (\beta_{k\ell}) \in \mathbb{R}^{K \times p}$  denote the matrices of signatures, activities, and regression coefficients, respectively. The integral in Equation (6) can be calculated via binning, leveraging the stepwise constant outputs from the assays used to extract genomic features; see Section 5.

We highlight that the model in Equation (5) differs from commonly employed regression approaches for inhomogeneous Poisson processes (Lawless, 1987). In these cases, one assumes an intensity function of the form  $\lambda(t) = \lambda_0(t) e^{\beta^\top \mathbf{x}}$ , where  $\lambda_0(t)$  is a baseline—either modeled as an explicit function of  $t$ , or in a fully nonparametric manner—while  $\beta$  are  $\mathbf{x}$  fixed quantities. Meanwhile, the intensity in Equations (3) and (5) handles covariates  $\mathbf{x}(t)$  and  $c_j(t)$  that vary with  $t$ . See Truccolo et al. (2005) for further examples relating Poisson processes to the generalized linear model framework. While further nonparametric approaches to capture the residual variations in mutation rate are possible (Lloyd et al., 2016) this is beyond our current inferential scope; see the further comments in Section 6.

## 2.4 PRIOR DISTRIBUTIONS

We now describe the priors over the parameters in Equations (3) to (5). Our choices closely follow the hierarchical model proposed in Zito and Miller (2024) based on *compressive hyperpriors*, which ensures automatic selection for the number of latent factors, provided that the rank  $K$  is chosen sufficiently large.

We begin by modeling each mutational signature  $r_k$  for each  $k = 1, \dots, K$  as

$$r_k = (r_{1k}, \dots, r_{Ik}) \sim \text{Dir}(\alpha_{1k}, \dots, \alpha_{Ik}), \quad (7)$$

where  $\text{Dir}(\alpha_1, \dots, \alpha_I)$  denotes the Dirichlet distribution with precision  $\alpha_1, \dots, \alpha_I$ , and  $\alpha_{ik} > 0$  are signature and channel-specific precisions. Equation (7) has two important advantages. First, it avoids the scaling ambiguities that arise in NMF, since  $\sum_{i=1}^I r_{ik} = 1$  for every  $k$ . Second, through the choice of  $\alpha_{ik}$  parameters, it enables the use of informative priors based on COSMIC or other signatures found in previous studies. In this case, the posterior returns an “updated” version of the previous signatures and may also discover novel ones. See also the *recovery-discovery* model of Grabski et al. (2025) for an additional example, and refer to Xue et al. (2024) for a method to tune  $\alpha_{ik}$  to resemble COSMIC signatures with a target cosine similarity.

As for the baseline activities  $\theta_{kj}$ , we adopt the following hierarchical priors:

$$(\theta_{k1}, \dots, \theta_{kJ} \mid \mu_k) \sim \text{Ga}\left(a, \frac{a}{\mu_k} \int_0^T \frac{1}{2} c_j(t) dt\right), \quad (8)$$

$$\mu_k \sim \text{InvGa}(aJ + 1, \varepsilon aJ), \quad (9)$$

where  $a > 0$  and  $\varepsilon > 0$  is a small constant such as  $\varepsilon = 0.001$ . Here,  $\text{Ga}(a, b)$  denotes a gamma distribution with mean  $a/b$  and  $\text{InvGa}(a_0, b_0)$  is an inverse gamma distribution with mean  $b_0/(a_0 - 1)$  whenever  $a_0 > 1$ . The hyperparameters  $\mu_1, \dots, \mu_K$  are referred to as *relevance weights* and each follows a data-dependent *compressive hyperprior*. Specifically,  $\mu_k$  controls the joint contribution of the activities  $\theta_{kj}$  in signature  $k$  across patients  $j = 1, \dots, J$ , adjusting for their total copy-number alterations. This is because  $\{\int_0^T \frac{1}{2}c_j(t)dt\} \times \mathbb{E}(\theta_{kj} | \mu_k) = \mu_k$  for each pair  $k, j$ . In turn, the inverse gamma hyperprior in Equation (8) ensures that (i) the relevance weights are centered at small values, since  $\mathbb{E}(\mu_k) = \varepsilon$ , and (ii) there is equal weight between the contribution from the exposures and that from the hyperprior since  $\mathbb{E}(\mu_k | \Theta) = \frac{1}{2}\varepsilon + \frac{1}{2}\sum_{j=1}^J \theta_{kj} \int_0^T \frac{1}{2}c_j(t)dt$ . If Equation (5) satisfies the setting of Proposition 1, then such a choice makes the posterior for each  $\mu_k$  and each  $\theta_{kj}$  concentrate at  $\varepsilon$  when signature  $k$  is redundant in the factorization, effectively removing it from the decomposition; see [Zito and Miller \(2024\)](#) for detailed descriptions and theory. In our empirical studies, we show how one still obtains a similar behavior in Equation (5), provided that  $K$  is larger than the true number of signatures in the data. Hence, Equation (8) removes redundant factors from the model, following a similar mechanism as the one in overfitted mixture models ([Rousseau and Mengersen, 2011](#)).

We conclude by specifying normal-inverse gamma priors for the regression coefficients as

$$\beta_k | \sigma_k^2 \sim \text{N}(\mathbf{0}, \sigma_k^2 I_p), \quad \sigma_k^2 \sim \text{InvGa}(c_0, d_0), \quad (10)$$

for each  $k = 1, \dots, K$ , where  $c_0, d_0 > 0$  and  $\text{N}(\boldsymbol{\xi}, \boldsymbol{\Sigma})$  is the  $p$ -variate normal distribution with mean  $\boldsymbol{\xi} \in \mathbb{R}^p$  and positive definite variance-covariance matrix  $\boldsymbol{\Sigma} \in \mathbb{R}^{p \times p}$ , and  $I_p$  is the  $p \times p$  identity matrix. Specifically, we set  $c_0 = 100$  and  $d_0 = 1$  as default values, making  $\beta_k$  highly concentrated at zero in the prior. This heavy shrinkage ensures that coefficients  $\beta_{k\ell}$  move away from zero when the signal from covariate  $\ell$  has good explanatory power for the mutation rate associated with the  $k$ th latent process.

### 3 POSTERIOR INFERENCE

This section presents two estimation algorithms for posterior inference in the PPF model: a maximum a posteriori (MAP) to obtain faster solutions, and a more expensive Markov chain Monte Carlo.

#### 3.1 MAXIMUM A POSTERIORI

The gold standard estimation strategy for NMF is first introduced in the influential work of [Lee and Seung \(2000\)](#) and consists of multiplicative updates derived from a majorization and then a minimization of the Kullback-Leibler loss. In simple terms, a majorizer for  $f(x)$  is a function  $g(y, x)$  of two arguments that satisfies two properties: (i)  $g(y, x) \geq f(y)$  at every  $y$ ; and (ii)  $g(x, x) = f(x)$  at every  $x$ . As a result, if  $y = \arg \min_z g(z, x)$ , then  $f(x) = g(x, x) \geq g(y, x) \geq f(y)$ . Hence, minimizing  $g$  implicitly minimizes  $f$  as well. This is advantageous when finding the minima of the majorizer is analytically simple, while finding those of the

---

**Algorithm 1.** MAP updates for the Poisson process factorization

---

**1 Signatures - for  $k = 1, \dots, K$  do**

 Update each probability  $r_{ik}$  for  $i = 1, \dots, I$  in signature  $k$  as

$$r_{ik} \leftarrow \frac{r'_{ik}}{\sum_i r'_{ik}} \quad r'_{ik} \leftarrow r_{ik} \left( \frac{\alpha_{ik} - 1}{r_{ik}} + \sum_j \sum_{n=1}^{N_{ij}} \frac{\theta_{kj} e^{\beta_k^\top \mathbf{x}(t_n)}}{\sum_{s=1}^K r_{is} \theta_{sj} e^{\beta_s^\top \mathbf{x}(t_n)}} \right);$$

**2 Baseline exposures - for  $j = 1, \dots, J$  and  $k = 1, \dots, K$  do**

 Update each  $\theta_{kj}$  as

$$\theta_{kj} \leftarrow \theta_{kj} \left( \frac{a - 1}{\theta_{kj}} + \frac{\mu_k}{\int_0^T \frac{1}{2} c_j(t) \{a + \mu_k e^{\beta_k^\top \mathbf{x}(t)}\} dt} \sum_i \sum_{n=1}^{N_{ij}} \frac{r_{ik} e^{\beta_k^\top \mathbf{x}(t_n)}}{\sum_{s=1}^K r_{is} \theta_{sj} e^{\beta_s^\top \mathbf{x}(t_n)}} \right);$$

**3 Regression coefficients - for  $k = 1, \dots, K$  do**

 Update the regression coefficients using Fisher scoring as  $\beta_k \leftarrow \beta_k - \mathbf{H}_k^{-1} \mathbf{g}_k$ , where

$$\begin{aligned} \mathbf{H}_k &= - \sum_j \theta_{kj} \int_0^T \frac{1}{2} c_j(t) e^{\beta_k^\top \mathbf{x}(t)} \mathbf{x}(t) \mathbf{x}(t)^\top dt - \frac{1}{\sigma_k^2} I_p \\ \mathbf{g}_k &= - \sum_j \theta_{kj} \int_0^T \frac{1}{2} c_j(t) e^{\beta_k^\top \mathbf{x}(t)} \mathbf{x}(t) dt + \sum_{ij} \sum_{n=1}^{N_{ij}} \frac{r_{ik} \theta_{kj} e^{\beta_k^\top \mathbf{x}(t_n)}}{\sum_{s=1}^K r_{is} \theta_{sj} e^{\beta_s^\top \mathbf{x}(t_n)}} \mathbf{x}(t_n) - \frac{1}{\sigma_k^2} \beta_k \end{aligned}$$

**4 Relevance weights and variances - for  $k = 1, \dots, K$  do**

 Update each parameter as  $\mu_k$  as

$$\mu_k \leftarrow \frac{a \sum_j \theta_{kj} \int_0^T \frac{1}{2} c_j(t) dt + \varepsilon a J}{2aJ + 1}, \quad \sigma_k^2 \leftarrow \frac{\beta_k^\top \beta_k / 2 + d_0}{p/2 + c_0 + 1}$$

**Output:** an updated point estimate for  $R, \Theta, B, \mu, \sigma^2$ .

---

original function is not. In our model, the target  $f$  is the negative log posterior

$$\begin{aligned} -\log \pi(R, \Theta, B, \mu, \sigma^2 \mid \{t_1, \dots, t_{N_{ij}}\}_{ij}) &= \\ &= \sum_{jk} \theta_{kj} \int_0^T \frac{1}{2} c_j(t) e^{\beta_k^\top \mathbf{x}(t)} dt - \sum_{ij} \sum_{n=1}^{N_{ij}} \log \left( \sum_{k=1}^K r_{ik} \theta_{kj} \frac{1}{2} c_j(t_n) e^{\beta_k^\top \mathbf{x}(t_n)} \right) \quad (11) \\ &\quad - \log \pi(R) \pi(\Theta \mid \mu) \pi(B \mid \sigma^2) \pi(\sigma^2), \end{aligned}$$

subject to  $\sum_{i=1}^I r_{ik} = 1$  for every  $k = 1, \dots, K$ , where the last line represents the prior distributions over model parameters presented in the previous sections. As we show in the Supplementary material, we can derive a majorizer for each argument  $r_k$ ,  $\theta_{kj}$  and  $\beta_k$  in Equation (11) leveraging the property that  $\log(\sum_{s=1}^S a_s) \geq \sum_{s=1}^S \eta_s \log(a_s/\eta_s)$  for any nonnegative weights  $\eta_1, \dots, \eta_k$  for which  $\sum_k \eta_k = 1$ . See [Lee and Seung \(2000\)](#).

Algorithm 1 presents the one cycle for the steps to minimize Equation (11). Specifically, Steps 1 and 2 update signatures and baseline activities in a multiplicative manner. Their relative simplicity follows because the minima of the majorizers of Equation (11) with respect to  $r_{ik}$  and  $\theta_{kj}$  are available analytically. Notice that signatures are re-normalized at each iteration due to the sum-to-one constraint of the Dirichlet prior.

Both updates ensure that the non-negativity requirements are automatically satisfied, provided that  $a \geq 1$  and  $\alpha_{ik} \geq 1$ . Hence, we recommend using  $a = \alpha_{ik} = 1.01$  as defaults. Instead, Step 3 is obtained by taking two intermediate steps. First, we majorize Equation (11) with respect to  $\beta_k$ . Then, we apply Newton’s method using the gradient  $\mathbf{g}_k$  and the Hessian matrix  $\mathbf{H}_k$  in each signature  $k$ . This second move is reminiscent of the Fisher scoring algorithm used in Poisson regression with the canonical logarithmic link (McCullagh and Nelder, 1989). Finally, the updates in Step 4 are simply the modes of inverse-gamma full conditionals.

Iterating Steps 1-4 until the relative difference between two successive evaluations of Equation (11) is lower than a given threshold, say  $10^{-7}$ , leads to a local optimum. While Equation (11) is guaranteed to decrease at every iteration, the final solution is not necessarily unique. This problem is an inherent characteristic of NMF; see Gillis (2020) for a review. Hence, we recommend initializing the algorithm from various random starting points and choosing the solution with the highest log posterior density. Furthermore, to avoid potential numerical instabilities, we repeat Step 3 twice at each iteration and update  $\beta_k$  as  $\beta_k \leftarrow \beta_k + \xi_k \min\{1, \rho\sqrt{p}/\sqrt{\sum_{\ell=1}^p \beta_{k\ell}^2}\}$  with  $\xi_k = -\mathbf{H}_k^{-1}\mathbf{g}_k$  and  $\rho > 0$ . This strategy is suggested by Miller and Carter (2020) and ensures that  $\beta_k$  moves along the direction  $\xi_k$  from Newton’s method while capping the root-mean-square of  $\xi_k$  at  $\rho$ . In our experiments, we find that  $\rho = 0.5$  works well in practice.

### 3.2 MARKOV CHAIN MONTE CARLO

The advantage of Algorithm 1 is that it returns point estimates relatively fast. However, in the context of our application, it is also useful to further obtain uncertainty quantification for the model parameters. This is especially true when assessing the relevance of a certain genomic covariate  $x_\ell(t)$  on the mutation rate associated with any latent process  $k$ . If the 95% posterior credible interval of the regression coefficient  $\beta_{k\ell}$  contains the origin, then we would have reason to believe that covariate  $x_\ell(t)$  does not significantly impact  $k$ . Moreover, we find that exploring the full posterior space yields more stable solutions in general.

Algorithm 2 describes a Markov chain Monte Carlo algorithm to obtain posterior samples from the model. In particular, we augment the likelihood by introducing one multinomial random variable for each observed mutation. Let  $W_{ij}(t_n) = \{W_{ij1}(t_n), \dots, W_{ijK}(t_n)\} \sim \text{Multinomial}\{1; p_{ij1}(t_n), \dots, p_{ijK}(t_n)\}$  and

$$p_{ijk}(t_n) = \mathbb{P}(W_{ijk}(t_n) = 1 \mid R, \Theta, B) = \frac{r_{ik}\theta_{kj}e^{\beta_k^\top \mathbf{x}(t_n)}}{\sum_{s=1}^K r_{is}\theta_{sj}e^{\beta_s^\top \mathbf{x}(t_n)}} \quad (12)$$

for the mutation at position  $t_n$ , with  $n = 1, \dots, N_{ij}$  and every channel-patient pair  $i, j$ . Then, conditionally on the matrix  $W \in \mathbb{R}^{\sum_{ij} N_{ij} \times K}$ , we can derive conjugate Dirichlet and gamma full conditionals for the signatures and the baseline activities, respectively; see Steps 2 and 3 in Algorithm 2. As for the regression coefficients, the full conditional in Step 3 is not from a known type. However, sampling can easily be performed using elliptical slice sampling (Murray et al., 2010) thanks to the Gaussian prior over  $\beta_k$ . This is a “rejection-free” sampler that works by proposing candidate points along the ellipse of the normal prior until an acceptable value is reached, using a threshold based on the sample from the previous iteration. Even though evaluations of the target are expensive in our application due to the large dimension of the genome, the method is advantageous since it does not require any tuning. Finally, the updates in Step 4 follow conjugate inverse gamma updates.

The quantity in Equation (12) represents the probability of assigning the mutation in channel  $i$  and patient  $j$  occurring at  $t_n$  to signature  $k$ . Unlike the standard multinomial data augmentation in Bayesian Poisson NMF

---

**Algorithm 2.** One cycle of the Gibbs sampler for the Poisson process factorization
 

---

1 **Latent attributions** - for  $i = 1, \dots, I$  and  $j = 1, \dots, J$  and  $n = 1, \dots, N_{ij}$  do

Sample the latent attribution for mutation at position  $t_n$  as

$$(W_{ij}(t_n) \mid R, \Theta, B) \sim \text{Multinomial}\{1; p_{ij1}(t_n), \dots, p_{ijK}(t_n)\}, \quad p_{ijk}(t_n) = \frac{r_{ik}\theta_{kj}e^{\beta_k^\top \mathbf{x}(t_n)}}{\sum_{s=1}^K r_{is}\theta_{sj}e^{\beta_s^\top \mathbf{x}(t_n)}}$$

2 **Signatures** - for  $k = 1, \dots, K$  do

Call  $M_{ik} = \sum_j \sum_{n=1}^{N_{ij}} W_{ijk}(t_n)$  the number of mutations of type  $i$  assigned to signature  $k$ .  
Sample  $r_k$  from

$$(r_k \mid W, B, \Theta) \sim \text{Dir}(\alpha_{1k} + M_{1k}, \dots, \alpha_{Ik} + M_{Ik}).$$

3 **Baseline exposures** - for  $j = 1, \dots, J$  and  $k = 1, \dots, K$  do

Call  $S_{kj} = \sum_i \sum_{n=1}^{N_{ij}} W_{ijk}(t_n)$  the number of mutations in patient  $j$  assigned to signature  $k$ .  
Sample  $\theta_{kj}$  from

$$(\theta_{kj} \mid W, B, R) \sim \text{Ga}\left(a + S_{kj}, \int_0^T \frac{1}{2} c_j(t) \left\{ \frac{a}{\mu_k} + e^{\beta_k^\top \mathbf{x}(t)} \right\} dt\right).$$

4 **Regression coefficients** - for  $k = 1, \dots, K$  do

Update the regression coefficients  $\beta_k$  using elliptical slice sampling (Murray et al., 2010) with target

$$\pi(\beta_k \mid \Theta, W, \sigma^2) \propto \exp\left\{-\sum_j \theta_{kj} \int_0^T \frac{1}{2} c_j(t) e^{\beta_k^\top \mathbf{x}(t)} dt\right\} \exp\left\{\sum_{ij} \sum_{n=1}^{N_{ij}} W_{ijk}(t_n) \beta_k^\top \mathbf{x}(t_n)\right\} \text{N}(\beta_k; 0, \sigma_k^2 I_p).$$

5 **Relevance weights and variances** - for  $k = 1, \dots, K$  do

Sample each  $\mu_k$  and  $\sigma_k^2$  from

$$(\mu_k \mid \Theta) \sim \text{InvGa}\left(a_0 + aJ, b_0 + a \sum_j \theta_{kj} \int_0^T \frac{1}{2} c_j(t) dt\right),$$

$$(\sigma_k^2 \mid B) \sim \text{InvGa}(c_0 + p/2, d_0 + \beta_k^\top \beta_k / 2).$$

**Output:** a sample from the joint posterior of  $B, \Theta, R$ , and  $\mu$ .

---

(Dunson and Herring, 2005; Zito and Miller, 2024), these probabilities are not constant, but vary along the genome depending on the specific behavior of the covariates. This is an important novelty: in our model, while it may be that a mutation of type  $i$  is attributed to process  $k$  in many loci, there might be regions where  $i$  is likely generated by another process  $k'$  instead.

## 4 SIMULATIONS

### 4.1 SETUP

We generate synthetic mutation data along an interval  $[0, T)$  and evaluate whether the use of covariates in the model improves inferences compared to the Poisson NMF model in Equation (1), which assumes a constant rate of mutation. We simulate covariates, copy numbers, model parameters, and mutations as follows.

**Covariates.** We consider an interval of length  $T = 200,000$  and divide it into equally-sized bins  $[\tau_q, \tau_{q+1})$  of length  $\Delta_q = \tau_{q+1} - \tau_q = 100$ , so that  $[0, T) = \cup_{q=1}^{Q-1} [\tau_q, \tau_{q+1})$  with  $\tau_1 = 1$  and  $\tau_Q = T$ . We simulate autocorrelated signals from  $\mathbf{z}_q \sim D\mathbf{z}_{q-1} + \mathbf{N}(\mathbf{0}, \Sigma_0)$  where  $D = \text{diag}\{0.99, \dots, 0.99\}$ ,  $\mathbf{z}_q \in \mathbb{R}^p$  and  $\Sigma_0 \in \mathbb{R}^{p \times p}$  is a chosen variance-covariance matrix. We then set  $\mathbf{x}(t) = (\mathbf{z}_q - \bar{\mathbf{z}})/\text{sd}(\mathbf{z})$  if  $t \in [\tau_q, \tau_{q+1})$ , where  $\bar{\mathbf{z}} = Q^{-1} \sum_{q=1}^Q \mathbf{z}_q$  and  $\text{sd}(\mathbf{z}) = \{(Q-1)^{-1} \sum_{q=1}^Q (\mathbf{z}_q - \bar{\mathbf{z}})^2\}^{1/2}$ , and “/” denotes the element-wise division. Hence, our hypothetical genome comprises  $Q = 20,000$  regions and has piecewise constant covariates with mean zero and variance one.

**Copy numbers.** To generate the copies  $c_j(t)$  in patients  $j = 1, \dots, J$ , we first randomly split  $[0, T)$  into  $n_j$  contiguous segments, with  $n_j \sim \text{Poisson}(20)$ , and then randomly allocate segment boundaries by drawing  $\tau_{j,s}$ ,  $s = 1, \dots, n_j$  uniformly among  $\tau_1, \dots, \tau_Q$ . The number of copies in each segment  $[\tau_{j,s}, \tau_{j,s+1})$  is then simulated from  $c_{j,s} \sim 2 + \text{NegBin}(1, 10)$ , where  $\text{NegBin}(m, v)$  denotes the negative binomial distribution with mean  $m$  and variance  $m(1 + m/v)$ . We set  $c_j(t) = c_{j,s}$  if  $t \in [\tau_{j,s}, \tau_{j,s+1})$ .

**Model parameters.** We define the true signature matrix  $R_0 \in \mathbb{R}^{I \times K_0}$  with  $I = 96$  by fixing the first four columns to the COSMIC signatures frequently appearing in breast cancer, namely SBS1, SBS2, SBS13 and SBS3; see Section 5 for a description of their etiology. The other columns are sampled from  $r_k^0 \sim \text{Dir}(0.1, \dots, 0.1)$ . Then, we generate the matrix of true baseline activities  $\Theta_0 \in \mathbb{R}^{K \times J}$  as  $\theta_{kj}^0 = \mu_k^0 \xi_{kj}^0 / \int_0^T \frac{1}{2} c_j(t) dt$ , with  $\mu_k^0 \sim \text{Ga}(100, 1)$  and  $\xi_{kj}^0 \sim \text{Ga}(0.5, 0.5)$ . Finally, we simulate the true coefficients by sampling  $\beta_k^0 \sim \mathbf{N}(\mathbf{0}, \sigma_0^2 I_p)$  for each  $k$ , with  $\sigma_0^2 = 1/2$  and call  $B_0 \in \mathbb{R}^{K \times p}$  the matrix with columns given by  $\beta_k$ .

**Mutations.** We allocate mutation along  $[0, T)$  for channel  $i = 1, \dots, I$  and patient  $J = 1, \dots, J$  by simulating  $I \times J$  Poisson processes using the inverse cumulative density function method. First, we sample the total number of mutations as  $N_{ij} \sim \text{Poisson}\{\Lambda_{ij}([0, T])\}$ , where  $\Lambda_{ij}([0, T]) = \int_0^T \lambda_{ij}(t) dt = \sum_{q=1}^Q \Delta_q \lambda_{ij,q}$ , and  $\lambda_{ij,q} = \sum_{k=1}^K r_{ik}^0 \theta_{kj}^0 \frac{1}{2} c_{jq} e^{\beta_k^{0\top} \mathbf{x}_q}$  with  $c_{jq}$  and  $\mathbf{x}_q$  being the copy number value and the covariates in the bin indexed by  $q$ . Then, we sample  $N_{ij}$  uniforms  $u_n \sim \text{U}(0, 1)$  for  $n = 1, \dots, N_{ij}$ , and for each realization we find the bin index  $q_n^*$  for which  $u_n \in [\sum_{q=1}^{q_n^*} \frac{\lambda_{ij,q}}{\Lambda_{ij}([0, T])}, \sum_{q=1}^{q_n^*+1} \frac{\lambda_{ij,q}}{\Lambda_{ij}([0, T])}]$ . Each  $t_n$  is drawn uniformly in  $[\tau_{q_n^*}, \tau_{q_n^*+1})$ .

**Simulation scenarios and tested models.** We take  $J = 40$  patients and  $p = 10$ , with  $K_0 = 8$  signatures (4 from COSMIC, 4 at random). However, we only use the first  $p_{\text{true}} = 5$  covariates to generate the mutations and set  $\beta_{k\ell} = 0$  for  $\ell = 6, \dots, 10$ . Hence, the last 5 covariates do not affect the mutation rate. We consider two scenarios: in Scenario A, we simulate genomic covariates as independent by setting  $\Sigma_0 = I_p$ ; in Scenario B, instead, we make them correlated by sampling  $\Sigma_0$  using the algorithm in function `genPositiveDefMat` with `covMethod = "onion"` from the R package `clusterGeneration`; refer to Joe (2006). This second case mimics the behavior of common genomic features, which often show high correlations; see Figure S2. The correlation structure introduces additional noise to the simulation, making the redundant covariates more similar to the one that generated the data. We sample 20 different datasets in each scenario, resulting in an average total number of mutations across replicates equal to 94,577 and 92,860 in Scenarios A and B, respectively. In each simulated dataset, we compare the outputs of the following models:

- (i) MAP, true – the MAP for the correctly specified model with  $c_j(t)$  set to the true values and  $p = p_{\text{true}} = 5$ .
- (ii) MAP, all  $\mathbf{x}$  – the MAP for the model with all  $p = 10$  covariates and the true values for  $c_j(t)$ .
- (iii) MCMC, all  $\mathbf{x}$  – the posterior mean for the same model in point (ii), starting from the MAP.
- (iv) MAP, CompNMF – the MAP of the model in Equation (1) with priors as in Zito and Miller (2024).

We set  $a = 1.01$ ,  $\alpha_{ik} = 1.01$ ,  $\varepsilon = 0.001$  and  $K = 15$ , and  $c_0 = 100$  and  $d_0 = 1$  in (i), (ii) and (iii). Additional comparisons against models considering copy-numbers only and coarser aggregations for the simulated covariates are reported in the Supplementary material.

## 4.2 SIMULATION RESULTS

We perform inference as follows. For models (i) and (ii), we run Algorithm 1 until the relative difference in log-posterior becomes lower than  $10^{-7}$ . For model (iv), we use the simpler multiplicative rules in Algorithm S1. In all cases, the starting point is generated by randomly drawing signatures from the symmetric Dirichlet prior in Equation (7) with  $\alpha_{ik} = 1.01$  and setting each baseline activity to  $\theta_{kj} = \sum_i N_{ij} / \int_0^T \frac{1}{2} c_j(t) dt$  for  $k = 1, \dots, K$ . We also initialize  $\beta_{k\ell}$  by drawing  $N(0, 10^{-7})$  when needed. As for model in (iii), we first estimate the MAP with Algorithm 1 and then use it as starting value for Algorithm 2, running one MCMC chain for 3,000 iterations and discarding the first 1,500 as burn-in. Run-times, number of iterations to reach convergence, and effective sample sizes in the full Bayesian inference case are reported in the Supplementary material.

Once the estimation procedure is completed, we post-process the output by eliminating redundant factors using the thresholding rule discussed in Zito and Miller (2024). Call  $\hat{\mu}_k$  and  $\hat{r}_k$  the posterior estimate for the  $k$ th relevance weight and the  $k$ th signature. These correspond to the posterior mode under Algorithm 1, and to the posterior mean under Algorithm 2. We discard all signatures for which  $\hat{\mu}_k \leq 5\varepsilon$  and the cosine similarity between  $\hat{r}_k$  and the uniform vector  $(1/96, \dots, 1/96)$  exceeds 0.975. In other words, a latent process is excluded from the factorization when its average activity is very close to  $\varepsilon = 0.001$  and the associated signature is constant. This returns an estimate for the number of active signatures  $\hat{K}$ . In both scenarios, all models retrieve  $\hat{K} = 8$ , except on a single dataset in Scenario A for model (ii). Moreover, signatures are retrieved with precision and sensitivity near one; see Figure S1.

For each case, we calculate  $\text{RMSE}(\hat{R}, R_0)$ ,  $\text{RMSE}\{\hat{\Theta}([0, T]), \Theta_0([0, T])\}$ , and  $\text{RMSE}(\hat{B}, B)$ , where  $\text{RMSE}(\hat{A}, A) = (\sum_{sh} (\hat{a}_{sh} - a_{sh})^2 / SH)^{1/2}$  denotes the root mean-squared errors between two matrices of generic dimension  $S \times H$ . Here,  $\Theta_0([0, T])$  is a matrix with entries calculated by integrating Equation (5) over  $[0, T]$ , and represents the total activity of each signature across the genome. Since this aggregate matrix is estimated by the standard NMF model in (iv), and signatures are pooled along the genome, comparing PPF and NMF for these estimates is meaningful. To calculate the RMSE, we first pad all matrices with zeros to avoid potential mismatches caused by differences in  $\hat{K}$  with respect to the true value. Then, we match signatures and the corresponding activities and regression coefficients against the truth using cosine similarity and the Hungarian algorithm.

Estimation performance for the data-generating parameters are displayed in the first three panels of Figure 2, plotted on the log scale to facilitate visualization. We notice the following. First, the RMSEs for  $R_0$  and  $\Theta_0([0, T])$  are considerably worse when covariates are not included, namely in (iv). This is surprising, since the model in Equation (1) is designed to estimate both quantities directly. Hence, even though the baseline NMF retrieves the correct number of signatures in every case with high precision, further adding covariates and copy numbers in the model improves inference for  $R_0$  and  $\Theta_0([0, T])$  as well. Second, the best performance is achieved by the MAP when the model is correctly specified—case (i), with  $p = p_{\text{true}} = 5$ . However, the addition of further redundant covariates in model (ii) does not strongly impact the retrieval of  $R$  and  $\Theta([0, T])$ , both in Scenarios A and B, except for a single outlier found in Scenario A for which  $\hat{K} = 9$ . Instead, the posterior mean for model (iii) appears to be a worse estimate, even though the chain was started precisely at the solution from model

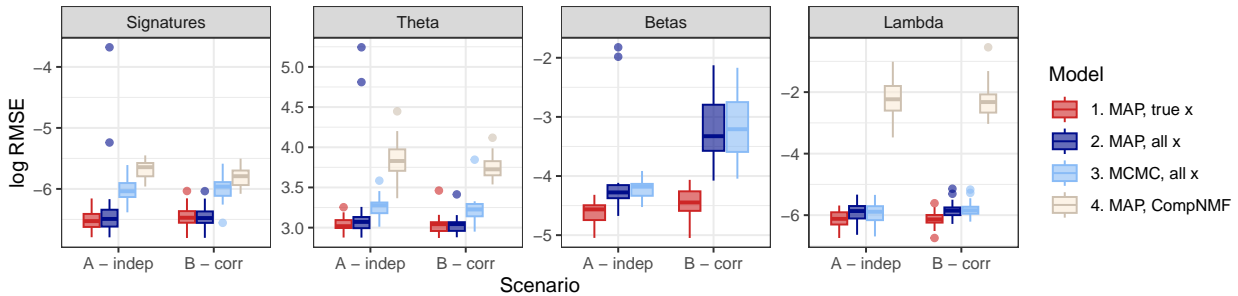


Figure 2: Results of the simulation described in Section 4.1 in terms of log RMSE for the parameters of the simulation. Boxplots display the values from 20 randomly generated datasets under both scenarios. The panel display, respectively,  $\log \text{RMSE}(\hat{R}, R_0)$ ,  $\log \text{RMSE}(\hat{\Theta}([0, T]), \Theta_0([0, T]))$ ,  $\log \text{RMSE}(\hat{B}, B_0)$  and  $\log \text{RMSE}(\hat{\Lambda}, \Lambda_0)$ .

(ii). Notice that running MCMC “corrects” the solution from the MAP, yielding  $\hat{K} = 8$  in all cases. Nevertheless, this difference virtually vanishes when estimating the regression coefficients  $B_0$  (third panel), suggesting that posterior mean and MAP yield a very similar  $\hat{B}$ . In this case, the correlated covariates in Scenario B lead to a considerable loss in performance in models (ii) and (iii) when compared to the correctly specified case (i).

In the fourth panel of Figure 2, we evaluate how well each model estimates the average intensity function in the data. We do so by calculating  $\text{RMSE}(\hat{\Lambda}, \Lambda_0) = (\sum_q (\hat{\Lambda}_{jq} - \Lambda_{jq})^2 / QJ)^{1/2}$  in each replicate, where  $\Lambda_{jq} = \sum_i \int_{\tau_q}^{\tau_{q+1}} \lambda_{ij}(t) dt$  is the total intensity in bin  $[\tau_q, \tau_{q+1})$ , and  $\hat{\Lambda}_{jq}$  is its estimated value. As expected, not incorporating covariates makes model (iv) again have the worst performance. Meanwhile, the RMSEs for models (ii) and (iii) are virtually identical. This implies that, despite the posterior mean being a worse estimate than the MAP for signatures and loadings, the difference in the estimated mutation rate over  $[0, T)$  is small.

## 5 APPLICATION: ICGC BREAST ADENOCARCINOMA

In this section, we apply our method to the breast adenocarcinoma dataset from Figure 1 using the genomic covariates in Table 1. In Section 5.1, we describe the pre-processing steps for all datasets. Then, we illustrate two ways in which one can use our model: a fully unsupervised version (Section 5.2) where signatures, activities, and regression coefficients are inferred *de novo*, and a version where known signatures from COSMIC are kept fixed (Section 5.3). Further details on data sources, additional analyses, and model diagnostics are reported in the Supplementary material.

### 5.1 DATA DESCRIPTION AND PRE-PROCESSING

We analyze whole-genome sequencing data from 113 women with breast cancer from the **Breast-AdenoCA** ICGC cohort of [The ICGC/TCGA Pan-Cancer Analysis of Whole Genomes Consortium \(2020\)](#).<sup>1</sup> The data consist of 707,104 mutations in total, for which we have access to the genomic location, comprising a chromosome and coordinate (e.g., `chrX:77364730-77364827`), and the single-nucleotide substitution with the flanking nucleotides (e.g., `A[C>T]C`). Patients are fairly heterogeneous: the median number of mutations aggregated across the 96 channels is 4,125, while there are also four *hypermuted* samples having more than 20,000 muta-

<sup>1</sup>Link to download: [https://pcawg-hub.s3.us-east-1.amazonaws.com/download/October\\_2016\\_whitelist\\_2583.snv\\_mnv\\_indel.maf.xena.nonUS](https://pcawg-hub.s3.us-east-1.amazonaws.com/download/October_2016_whitelist_2583.snv_mnv_indel.maf.xena.nonUS)

tions, with a maximum of 64,464 (patient DO1076). We also have access to data on copy number alterations, which are calculated by ensembling six different copy-number calling algorithms.<sup>2</sup> In simple terms, copy number frequencies indicate the estimated number of copies of each segment of the genome present in a single tumor cell for a given individual, with 2 being the value for a normal cell. Patients featured missing values for the copy number in some regions, with a total length of approximately 46Mb on average across the sample ( $< 1.5\%$  of the total genome length). In this case, we substitute the missing values with a 2, assuming normal conditions. Importantly, variations in copy number are correlated with the mutation rate at the Mb scale ( $\text{cor} = 0.44$ ,  $p < 2.2 \times 10^{-16}$ ). For example, the average copy numbers in chromosome arms 1p and 1q are 2.42 and 3.90, respectively, with associated average mutation counts equal to 217 and 304, across all patients. This explains the “jump” in Figure 1 for chromosome 1.

We assemble the covariates in Table 1 from various sources; see Table S3. Specifically, we consider a similar set of data to the one previously analyzed by [Otlu et al. \(2023\)](#), whose goal is to study the relationship between epigenetic markers and mutational signatures explicitly. To do so, we download from ENCODE all the `bigWig` files associated with the `bed` files indicated in the supplement of [Otlu et al. \(2023\)](#). While `bed` files report the regions having statistically significant enrichments from a covariate, `bigWig` formats contain the signal for the whole genome; hence, they are better suited for our application. We use the files that measure the fold-change over control from the ChIP-seq assay for both histone modifications and CTCF binding. This unit of measurement has a more transparent interpretation as opposed to  $-\log_{10}$  p-values, which is instead used for visualization purposes and to identify significant peaks. Replication timing is obtained from data on the MCF-7 breast cancer cell line, as in [Morganella et al. \(2016\)](#). As for nucleosome occupancy, we use data from an MNase-seq assay on the K562 leukemia cell line ([Tolstorukov et al., 2011](#)). Despite not being breast-specific, it is one of the few datasets on nucleosome position that is cancer-specific ([Otlu et al., 2023](#)). Finally, methylation data are obtained from [Loyfer et al. \(2023\)](#) and migrated from genome `hg38` to `hg19` using `liftOver`.

Our pre-processing steps are the following. We subdivide chromosomes 1 to 22 and X in the `hg19` genome into non-overlapping regions of 2,000 nucleotides (2kb aggregation) via the `tileGenome` function in the R package `GenomicRanges` ([Lawrence et al., 2013](#)). Chromosome Y is excluded because all patients are female. We assign to each bin a weight  $\Delta_q$ , calculated as the number of nucleotides in a region, excluding the portions that overlap with any of the problematic regions listed by [Amemiya et al. \(2019\)](#). Hence, if a region is not problematic and does not have any missing values “N”, we have  $\Delta_q = 2,000$ . Meanwhile,  $\Delta_q = 0$  implies that no mutation can be detected in that bin. We subdivide the copy number data for each patient using the same partition, and call  $c_{jq}$  the number of copies for patient  $j$  in bin  $q$ . As for the covariates, we first import into memory each `bigWig` file in Table S3 using the `rtracklayer` package ([Lawrence et al., 2009](#)) and then calculate the average value of the signal in every bin using the function `binnedAverage` in `GenomicRanges`. Signals from different files representing the same covariate are then averaged in each bin. As for GC content, we simply calculate the fraction of G and C in the 2kb bins via the function `letterFrequency` in the package `Biostrings` ([Pagès et al., 2023](#)). This results in 11 piecewise constant covariates aligned to the same coordinates, with a total of  $Q = 1,391,345$  bins having a non-zero weight  $\Delta_q > 0$  and with  $T = \sum_q \Delta_q = 2,780,909,076$ . This is lower than the overall length of `hg19` due to the presence of blacklisted regions. Finally, we cap the value of all covariates

---

<sup>2</sup>Link to download: [https://pcawg-hub.s3.us-east-1.amazonaws.com/download/20170119\\_final\\_consensus\\_copynumber\\_donor](https://pcawg-hub.s3.us-east-1.amazonaws.com/download/20170119_final_consensus_copynumber_donor)

at their 99.9th percentile to avoid excessively long tails, and we standardize them to have a mean of zero and a variance of one across bins.

We highlight that the covariates under analysis are *not* patient-specific, but instead correspond to a *reference epigenome* that is common to all patients. Moreover, except for nucleosome occupancy and replication timing, all assays are run on tissues and cell lines from breast epithelium obtained from a separate group of healthy donors. Hence, our analysis detects associations that reflect mutational biases in the cancer genomes that are not driven by patient-specific alterations in the chromatin. Moreover, the 2kb scale is motivated by the need to balance between information at the original **bigWigs** resolution, and computational feasibility when running estimation algorithms. In particular, when  $A = [0, T)$ , the integral in Equation (6) is equal to

$$\int_0^T \frac{1}{2} c_j(t) e^{\beta_k^\top \mathbf{x}(t)} dt = \sum_{q=1}^Q \Delta_q \frac{1}{2} c_{jq} e^{\beta_k^\top \mathbf{x}_q},$$

where  $\mathbf{x}_q$  and  $c_{jq}$  denote the constant values of the covariates and the copy numbers in each bin. Using finer partitions leads to heavier computations and memory requirements, while coarser partitions may obscure the effect of covariates operating at smaller scales, such as CTCF. Furthermore, a 2kb window size centered at each mutation ( $\pm 1000$  bases) is the proposed size in the analyses of [Otlu et al. \(2023\)](#) when analyzing mutational signatures contributions near histone modification and transcription factors.

## 5.2 DE NOVO ANALYSIS

### 5.2.1 ESTIMATION STRATEGY AND RECONSTRUCTION ERRORS

To assess the impact of the covariates on the latent factors, we estimate a fully unsupervised PPF model with  $a = 1.01$  and  $\varepsilon = 0.001$  in Equation (8), and  $\alpha_{ik} = 1.01$  in Equation (7) for each  $i$ , setting  $K = 12$  as an upper bound. All signatures are the same *a priori* and no information from the COSMIC signatures is incorporated in the model, unlike previous analyses ([Zito and Miller, 2024](#); [Grabski et al., 2025](#)).

We first run Algorithm 1 from three different starting points generated at random via the initialization strategy in Section 4.2, stopping the updates when the relative difference in log-posterior falls below  $10^{-7}$ . This step took, respectively, 1,379, 2,739, and 1,409 iterations to complete in parallel, over a total of 211, 367, and 215 minutes (average of 9 seconds per iterations) on an AMD Ryzen 3900-based dedicated server with 128GB of memory, running Ubuntu 20.04, R version 4.3.1 linked to Intel MKL 2019.5-075. All three runs detect very similar sets of signatures: the average cosine similarity between each pair of solutions is 0.9 after matching the columns via Hungarian algorithm. Moreover, the number of signatures for which  $\hat{\mu}_k^{\text{MAP}} > 1.5\varepsilon$  was, respectively, 10, 9, and 9. In few cases, some signatures had relevance weight  $\hat{\mu}_k^{\text{MAP}} \approx \varepsilon$ , but  $\hat{\beta}_k$  was not equal to zero. We then chose the solution having the highest log-posterior as initial value for Algorithm 2, and ran 10,000 Markov chain Monte Carlo iterations, using the last 3,000 samples to calculate posterior means and 95% credible intervals for each parameter. Our final solution has  $\hat{K} = 9$  signatures. Interestingly, we always found that  $\hat{r}_{ik}^{\text{MCMC}} \approx 1/96$  (a uniform) and  $\hat{\beta}_k^{\text{MCMC}} \approx \mathbf{0}$  when  $\hat{\mu}_k^{\text{MCMC}} \leq 1.5\varepsilon$ . This suggests that when a signature has relevance weight  $\hat{\mu}_k^{\text{MAP}} \approx \varepsilon$  but  $\hat{r}_k^{\text{MAP}}$  is not uniform and  $\beta_k^{\text{MAP}}$  is not near zero, it is likely a spurious artifact of the optimization.

Our method reconstructs the aggregated mutation counts well, with  $\text{RMSE}(\hat{\Lambda}, N) = 14.01$ , where  $\hat{\Lambda}$  is estimated via Equation (6) with  $A = [0, T)$ , and  $N$  is the matrix of total mutations in Section 2.1. We

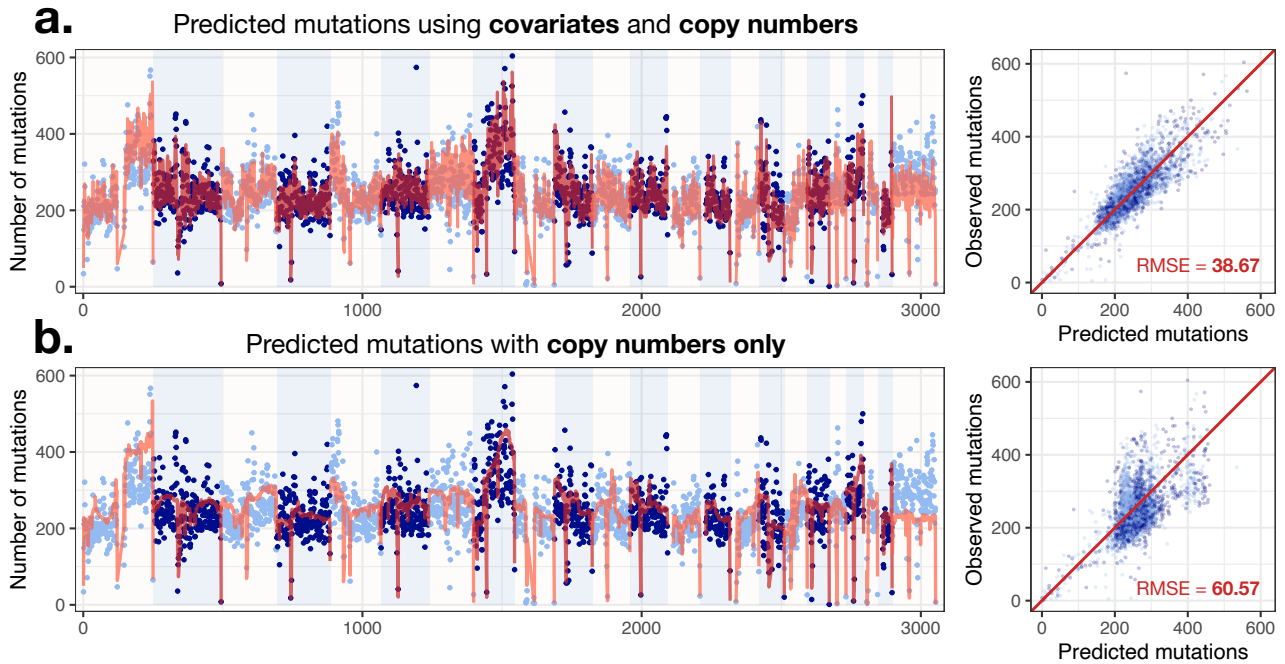


Figure 3: True and predicted total number of mutations from the PPF model at the megabase scale. Left: total mutations (points) and estimated total intensity (line); alternating colors and bands indicate chromosomes. Right: scatterplot of true and predicted values. **a.** PPF predictions using covariates from Table 1 and data on individual copy numbers. **b.** PPF predictions using only data on individual copy numbers, without covariates.

compare this to the NMF solutions from CompNMF (Zito and Miller, 2024) and SignatureAnalyzer (Kim et al., 2016). Both of these models allow for automatic choice of the number of latent factors, making them an ideal benchmark. Their estimated numbers of signatures are 5 and 9, respectively, with reconstruction errors of 14.63 and 13.37. This indicates that our method has comparable performance to those designed to directly reconstruct the total counts. To test reconstruction at finer scales, we also run Algorithm 1 with copy numbers only. As illustrated in Figure 3, the use of covariates improves the reconstruction of the total number of mutations at the megabase scale.

### 5.2.2 INFERRED LATENT PROCESSES AND COVARIATE EFFECTS

Figure 4a reports the posterior mean and credible intervals for the inferred signatures. Values in parentheses on the left indicate the closest COSMICv3.4 signature in terms of cosine similarity. We see that our model recovers both APOBEC-related signatures: Sig4 is a perfect match to SBS2, while Sig1 matches SBS13 in COSMICv3.4 with a score of 0.86, which however becomes 0.99 in COSMICv2, an earlier version of the database. Overall, the similarities are moderate-to-high, except for Sig8, whose similarity to SBS98 is too low for a confident attribution. Sig2 and Sig3 also have large contributions to the mutation rate, as displayed by the size of the relevance weights  $\hat{\mu}_k$  in Figure 4b. Sig2 matches with SBS5, which is associated with aging (Alexandrov et al., 2015), while Sig3 is close to SBS40A, which is ubiquitous in tumors (Alexandrov et al., 2020). Moreover, we find moderate evidence of SBS3 (Sig5), SBS18 (Sig 7), and SBS10B (Sig9): these are important signatures in breast cancer, related to homologous recombination deficiencies (HRD), reactive oxygen species (ROS), and POLE

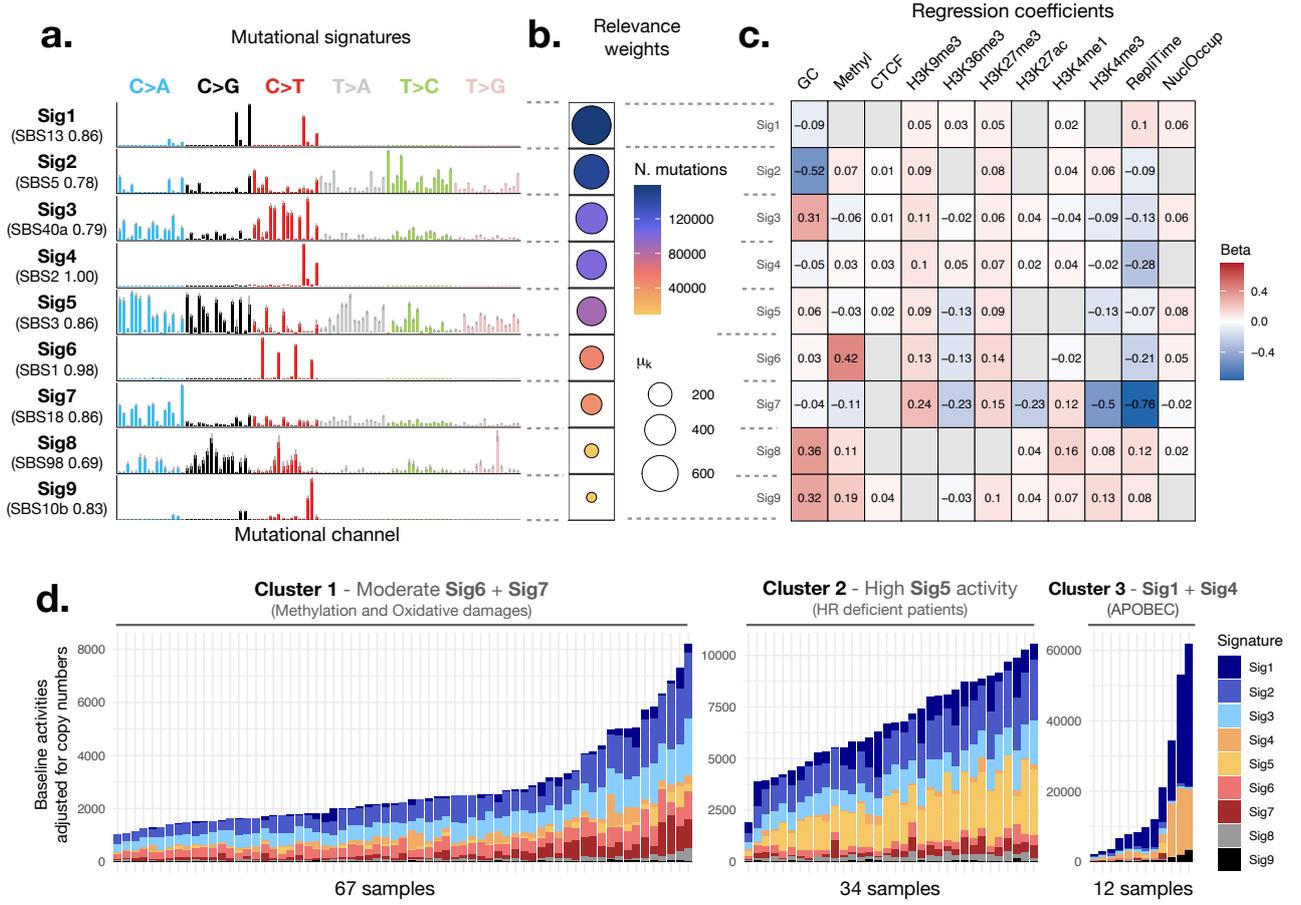


Figure 4: Estimates for the parameters in the PPF model. **a.** Posterior mean for the *de novo* mutational signatures. The gray bars indicate 95% posterior credible intervals. Numbers in parentheses on the left indicate the highest cosine similarity in the COSMICv3.4 catalog. **b.** Posterior mean of the relevance weights  $\hat{\mu}_k$  associated with each signature, with larger point size indicating larger values. For each signature, the color intensity denotes the number of mutations in the data for which that signature has the highest assignment probability in Equation (12). **c.** Posterior mean of the regression coefficients,  $\hat{\beta}_k$ . Gray cells with no number indicate estimates for which the 95% posterior credible interval contains zero. **d.** Baseline activities  $\hat{\theta}_{kj}$  adjusted by total copy numbers for each signature. Each column corresponds to a patient, and the three panels indicate the three clusters inferred from the normalized activities.

exonuclease (a process leading to hypermutation), respectively. As we further comment below, we also recover SBS1 with high accuracy.

As for the exposures in each patient, Figure 4d displays the baseline activities adjusted for the copy numbers, namely  $\theta_{kj} \int_0^T \frac{1}{2} c_j(t) dt$ , in every signature-patient combination. To understand the broader impact of each latent process, we perform a cluster analysis on a normalized version of these activities, selecting the optimal number of clusters by minimizing the silhouette score. This procedure identified three distinctive groups: a large cluster characterized by relatively large exposures to methylation-driven mutations and ROS damages (Cluster 1 - Sig6 and Sig7), a medium-sized cluster with a high exposure to SBS3 (Cluster 2 - Sig5), and a small APOBEC-related cluster (Cluster 3 - Sig1 and Sig4, and the hypermutated patients with Sig9). Notably, Cluster 2 exhibits signs of HRD, for which PARP inhibition therapies have proven particularly effective (Gulhan et al., 2019).

Further insights into the mutational processes are clearly provided by Figure 4c, which shows the posterior mean of regression coefficients  $\hat{\beta}_k$ . Since we standardized the covariates, all values are on the same scale. The

intensity of the color of each cell indicates the magnitude of the coefficient, while gray cells without numbers are those where the 95% posterior credible intervals contain zero. We highlight the following important findings:

- 1. Methylation enables clean recovery of SBS1 and lowers the mutation rates for C>A-enriched signatures.** Indeed, signature Sig6 shows a cosine similarity with SBS1 of 0.98, indicating almost perfect matching. In turn, its coefficient for methylation is large and positive (0.42). This is consistent with the proposed biological mechanism, namely C>T mutations arising from methylated CpG sites. Meanwhile, Figure S3 in the Supplementary material shows that both CompNMF and SignatureAnalyzer recover a contaminated version of SBS1: CompNMF finds one signature that matched with 0.82 cosine similarity, while SignatureAnalyzer finds two SBS1-like signatures with 0.83 and 0.80 similarity. Contamination of SBS1 with other signatures, especially SBS5, is a rather common problem in many tools due to their correlated exposures (Wu et al., 2022). However, using methylation as a covariate solves the issue in our model. Interestingly, Sig3, Sig5, and Sig7, which all feature a high probability of C>A substitutions, are inversely associated with methylation. Since we are using 2kb binning with piecewise constant covariate values, this suggests that being in areas near methylated sites may lead to lower activities from other processes, particularly oxidative stress and HR deficiencies.
- 2. Late replication timing leads to large increases in mutational burden, but some signatures are enriched in early replicating regions.** The link between replication timing and mutation rate is well established (Dietzen et al., 2024). Similarly, our inferred signatures show relatively large coefficients for this covariate compared to others, with Sig7, Sig4, and Sig6 being the most affected. Notice that, by construction, *negative small values* in our analysis indicate *late* replication timing, while *positive* ones imply that a region is replicating *early*. Hence, we find that a one standard deviation increase in late replication timing translates into a 113% increase in the expected mutations arising from oxidative damages (Sig7,  $e^{0.76} - 1 \approx 1.13$ ), leads to a 23% increase in mutation intensity from SBS1 (Sig6,  $e^{0.21} - 1 \approx 0.23$ ), and produces a 32% increase in the faulty APOBEC signature SBS2 (Sig 4,  $e^{0.28} - 1 \approx 0.32$ ), holding all other covariates constant. On the other hand, the other APOBEC-related signature, Sig1, appears moderately enriched at early replicating areas (positive coefficient).

It is worth highlighting that current approaches like SigProfilerTopography assess the impact of replication timing by tiling the total genomic signal into deciles and counting the number of mutations from a signature belonging to each bin. Then, one tests for the difference between this partition and the one obtained by placing mutations at random genomic locations; see Otlu and Alexandrov (2025) for details. Instead, our model bypasses this procedure by providing a direct measurement for the impact of each covariate while retaining the intuitive interpretation of a standard log-linear model. Additionally, mutations are typically assigned to a signature only if their attribution probability exceeds a certain threshold (e.g., 90%), leading to a loss of information. For instance, COSMIC currently reports that SBS10B is mildly enriched at later replicating areas in colorectal and endometrial cancer, but does not provide results for breast cancer. Interestingly, we find that our signature Sig9, despite being active in only a few patients, has the opposite behavior when accounting for all other covariates.

- 3. All activities increase in heterochromatic domains and vary at active enhancers and promoters.** In fact, H3K9me3 and H3K27me3, which are markers for heterochromatin and gene suppression,

respectively, have nonnegative coefficients for every signature. Meanwhile, we find that H3K36me3 has a rather strong depleting effect on Sig5, Sig6 and Sig7. This is due to the encoded repair mechanism for mismatches led by this histone mark, which corrects mutational damages (Li et al., 2013). Interestingly, H3K36me3-rich regions have been found to be enriched after exposure to carcinogens, such as tobacco smoking or alcohol (Supek and Lehner, 2017). We find that the APOBEC signatures Sig1 and Sig4 exhibit a mild positive association with H3K36me3, though with small variations (3% and 5% increase, respectively). The effects of H3K4ac, H3K4me1, and H3K4me3, which are markers for enhancers and promoters and favor gene activity, differ across signatures. In particular, Sig7 and Sig5 are the most affected by H3K4me3. Finally, several signatures are slightly positively associated with the presence of CTCF sites; here, the small coefficients might be due to the 2kb aggregation, since this mark operates at smaller scales.

4. **GC content has a strong, varied effect on several signatures.** This is evident from the magnitude of the coefficients in Sig2, Sig3, and Sig8, whereas the other spiky signatures are less impacted, except for Sig9.

### 5.3 ANALYSIS WITH KNOWN SIGNATURES

Besides *de novo* analysis, signature *refitting* is also a common practice when studying mutational signatures (Díaz-Gay et al., 2023). The goal is to estimate the activities of known signatures based on the observed mutation counts, often done using non-negative least squares. Since many COSMIC signatures are byproducts of known biological processes, this procedure allows for a clear interpretation of their specific impact. By fixing the signatures to known values, our PPF model can be used as a tool for covariate-dependent refitting.

To test the effect of known signatures, we consider a PPF with  $K = 13$  and with the same covariates as Table 1, but where  $r_1, \dots, r_K$  are set to the following COSMICv3.4 members: two aging signatures (SBS1 and SBS5); two APOBEC-related signatures (SBS2 and SBS13); three associated with mismatch repair deficiencies (SBS6, SBS20, and SBS26); three related to oxidative damages (SBS18, SBS17A, and SBS17B); two HRD-related signatures (SBS3 and SBS8); and one related to base excision repair deficiency (SBS30). An earlier version of these signatures was previously analyzed by Morganella et al. (2016), who first explored their relationship with epigenetic marks in breast adenocarcinoma.

We modify Algorithm 2 to skip the updates to the signatures  $r_k$  (Step 2), and run it for 10,000 iterations with randomly initialized activities, discarding the first 2,000 iterations as burn-in, with  $a = 1.01$  and  $\varepsilon = 0.001$ . Figure 5a reports the posterior mean for the regression coefficients  $\hat{\beta}_k$  associated with each signature, and the relevance weights  $\hat{\mu}_k$ . The “×” mark in SBS6, SBS20, SBS26, and SBS17a indicates that  $\hat{\mu}_k \approx \varepsilon$ . These last three signatures have all their regression coefficients shrunk to zero, making their contribution to the decomposition virtually irrelevant. A minor exception is SBS6, for which GC content, H3K27ac, and H3K4me3 have non-zero coefficients. This suggests that there is a small signal from the signature that the model is capturing. Interestingly, the values for  $\hat{\beta}_k$  for SBS1 closely resemble the estimates from the *de novo* results in Figure 4c, where Sig6 corresponds to SBS1. We also observe an enrichment at early replication timing for SBS3 and SBS13, which is different from previous analyses (Morganella et al., 2016). For all signatures, we still detect increased mutation rates in association with heterochromatic markers H3K9me3 and H3K27me3, while the

effect of H3K36me3 is varied but mostly negative. As before, the largest contributors to the decomposition are SBS2, SBS3, SBS5, and SBS13, and GC content exhibits relatively large effects. Finally, SBS8 and SBS17b have fairly strongly correlated coefficients, with signs usually being both positive or both negative. However, the total contribution of SBS17b appears to be considerably smaller. Neither signature was detected in the previous analysis.

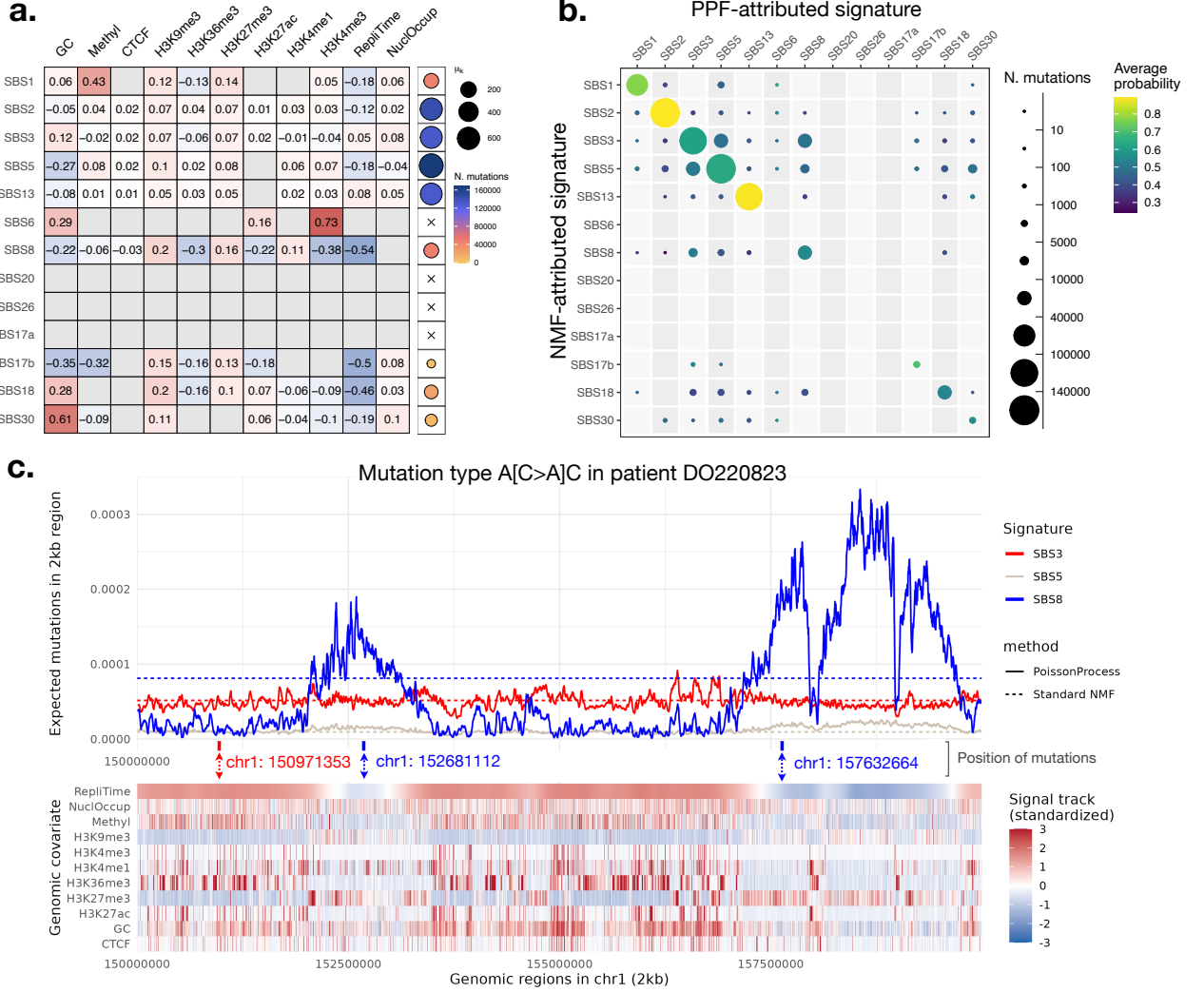


Figure 5: Signature refitting results. **a.** Regression coefficients and relevance weights for the signatures in the analysis. Gray boxes indicate entries where the 95% posterior credible interval contains zero. The  $\times$  marks indicate cases where  $\hat{\mu}_k \approx \varepsilon$ . **b.** Number of mutations attributed to a signature in the standard NMF case (y-axis) and in the PPF model (x-axis). **d.** Top panel: mutation intensity for SBS3, SBS5, and SBS8 on mutational channel A[C>A]C in patient DO220823 in genomic region chr1:15000000-16000000. The three ticks indicate the exact mutation position. Solid and dashed lines indicate the intensity from the PPF and the CompNMF model with fixed signatures, respectively. Bottom: standardized values for the covariates in the region.

As described in Section 3.2, an important aspect of our model is that we can calculate mutation-specific signature attribution probabilities, using the data augmentation strategy in Equation (12). Hence, we can attribute a mutation to a signature by assigning it to the latent process having the highest probability. In the baseline NMF in Proposition 1, Equation (12) becomes equal at every location  $t_n$  for a given triplet  $i, j, k$  since  $\beta_k = \mathbf{0}$ . To test how genomic covariates affect classification, we estimate the assignment probabilities

of the CompNMF model (Algorithm S1) with the same set of fixed signatures, and compute the attribution probabilities of each mutation. The results are displayed in Figure 5b, which reports the number of mutations attributed to each signature in both models and the average assignment probabilities for these mutations. We see that the majority of mutation attributions are consistent between the two models, as demonstrated by the large values on the main diagonal. However, 95,042 mutations (13.2% of the total) appear to have a different attribution, though the classification probabilities are lower on average.

One specific example is given by the important differences between the two models with respect to SBS3, SBS8, and, to a lesser extent, SBS5. The first two signatures show a similar pattern of mutations at C>A and T>A motifs, which naturally leads to a higher *a priori* uncertainty in the attribution probability. Indeed, SBS8 has been posited to originate from homologous recombination deficiencies, but, unlike SBS3, experimental validation for the claim has not been achieved yet. In Figure 5c, which displays the posterior for the intensity function in region `chr1:150000000-160000000` for patient DO220823 and mutation type  $i = A[C > A]C$ , we see that such unclear attribution might be related to a higher propensity of SBS8 to appear in heterochromatic regions characterized by later replication timing. The three ticks between the facets indicate the genomic position where mutations were detected in the region. We smoothed the intensity using a rolling mean with a 10-region window to aid visualization. Our model attributes the first mutation to SBS3, since it falls in an area characterized by early replication timing, with strong peaks of H3K36me3 and low values of H3K9me3 and H3K27me3. Meanwhile, the other two mutations are detected in regions of predominantly late replication timing, which causes a spike in activity for SBS8. Interestingly, this activity drops dramatically when H3K36me3 is high, which leads to the two dips in the predicted SBS8 activity following the third mutation. Hence, our results validate the recent findings of Singh et al. (2020) about SBS8, showing the advantages of the PPF framework.

## 6 DISCUSSION

Mutational signature analysis is now routinely performed in studies of tumors with available whole-genome or whole-exome sequencing data, and remains an area of active methodological development. The method presented in this article further extends the literature by proposing a model that enables joint inference on mutational signatures and their dependence on genomic features where mutations are observed, including histone modifications, transcription factors, GC content, DNA methylation, and copy number alterations. Our analyses illustrate how adding covariates to the factorization favors interpretability, while also improving the detection of signatures. Furthermore, the model naturally provides position-specific probabilities for each signature, which allows us to attribute any mutation to a signature based on genomic context and covariates.

In our model, signatures are held constant across the genome, while covariate-dependent activities capture all regional variations. However, many COSMIC signatures display asymmetries with respect to replication strand (Otlu et al., 2023). This effect can be modeled by making signatures further depend on genomic coordinates, paired with, for instance, hierarchical Dirichlet priors over strand-specific hyperparameters. Additionally, our analyses considered covariates from a *reference epigenome* common to all patients, with the exception of patient-specific copy numbers. Nevertheless, our framework can be adapted to incorporate patient-specific regression coefficients, to also control for the effect of chromatin accessibility (Corces et al., 2018) and gene expression on

mutations. Both extensions are attainable with minor modifications to the model and have the potential to offer novel insights into the mutational processes in cancer genomes.

There are many interesting directions worth exploring in the near future. One possibility is to further leverage the connection between generalized linear models and the Poisson process factorization in a nonparametric manner. Borrowing from the exciting emerging literature on spatial factorization methods for transcriptomics (Townes and Engelhardt, 2023; Wang et al., 2024; Laursen et al., 2025), we can further extend the model using a Cox process, that is, specifying Gaussian process priors over signature exposures. For instance, one can construct a covariance matrix using Hi-C contact matrices, which measure the intrachromosomal distance between genomic regions in three dimensions (Lieberman-Aiden et al., 2009). Recent analyses suggest that the spatial folding of chromatin plays a key role in shaping the mutational landscape of cancer genomes (Akdemir et al., 2020; Yost et al., 2025), though these data have not yet been used in the NMF context.

A second direction consists of applying the mutation intensity estimated by our model to identify driver mutations in cancer genes. Prominent methods like MutSigCV (Lawrence et al., 2013) and Dig (Sherman et al., 2022) perform this task by estimating an expected background mutation rate and then comparing it against the observed mutation rate. Regions and genes with statistically significant differences are then identified as cancer drivers. In this regard, the residual difference between the real mutations at the kb scale and the intensity function in PPF is informative of regions presenting anomalies not explained by the covariates. Finally, the supervised version of the PPF discussed in Section 5.3 is an interesting regression framework. Studying the identifiability of the activity parameters is an important next direction, which has potential applications in causal analyses for latent outcomes (Landy et al., 2025).

## ACKNOWLEDGEMENTS

We are deeply grateful to Mehmet Samur, Jenna Landy, and Catherine Xue for the many helpful discussions. J.W. Miller and A. Zito were supported in part by the National Cancer Institute of the NIH under award number R01CA240299. G. Parmigiani and A. Zito were supported by grant number 5R01CA262710-05. The content is solely the responsibility of the authors and does not necessarily represent the official views of the National Institutes of Health. A. Zito also acknowledges support from Paula and Rodger Riney Foundation.

## CODE AVAILABILITY

Code to run the method and reproduce the results in the article is publicly available at <https://github.com/alessandrozito/SigPoisProcess>.

## REFERENCES

- Abascal, F., R. Acosta, N. J. Addleman, et al. (2020). Expanded encyclopaedias of DNA elements in the human and mouse genomes. *Nature* 583(7818), 699–710.
- Aguirre, A. J., J. A. Nowak, N. D. Camarda, et al. (2018). Real-time genomic characterization of advanced pancreatic cancer to enable precision medicine. *Cancer Discovery* 8(9), 1096–1111.

- Akdemir, K. C., V. T. Le, J. M. Kim, et al. (2020). Somatic mutation distributions in cancer genomes vary with three-dimensional chromatin structure. *Nature Genetics* 52(11), 1178–1188.
- Alexandrov, L. B., P. H. Jones, D. C. Wedge, J. E. Sale, P. J. Campbell, S. Nik-Zainal, and M. R. Stratton (2015). Clock-like mutational processes in human somatic cells. *Nature Genetics* 47(12), 1402–1407.
- Alexandrov, L. B., J. Kim, N. J. Haradhvala, et al. (2020). The repertoire of mutational signatures in human cancer. *Nature* 578(7793), 94–101.
- Alexandrov, L. B., S. Nik-Zainal, D. C. Wedge, et al. (2013). Signatures of mutational processes in human cancer. *Nature* 500(7463), 415–421.
- Amemiya, H. M., A. Kundaje, and A. P. Boyle (2019). The ENCODE blacklist: Identification of problematic regions of the genome. *Scientific Reports* 9(1), 9354.
- Benjamin, D., T. Sato, K. Cibulskis, G. Getz, C. Stewart, and L. Lichtenstein (2019, January). Calling somatic SNVs and indels with Mutect2. *bioRxiv*, 861054.
- Bird, A. P. (1980, 04). Dna methylation and the frequency of cpg in animal dna. *Nucleic Acids Research* 8(7), 1499–1504.
- Blokzijl, F., R. Janssen, R. van Boxtel, and E. Cuppen (2018). Mutational patterns: comprehensive genome-wide analysis of mutational processes. *Genome Medicine* 10(1), 33.
- Corces, M. R., J. M. Granja, S. Shams, et al. (2018). The chromatin accessibility landscape of primary human cancers. *Science* 362(6413), eaav1898.
- Daley, D. J. and D. Vere-Jones (2003). *An introduction to the theory of point processes. Vol. I* (Second ed.). Probability and its Applications (New York). New York: Springer-Verlag.
- Díaz-Gay, M., R. Vangara, M. Barnes, et al. (2023). Assigning mutational signatures to individual samples and individual somatic mutations with SigProfilerAssignment. *bioRxiv*.
- Dietzen, M., H. Zhai, O. Lucas, O. Pich, C. Barrington, W.-T. Lu, S. Ward, Y. Guo, R. E. Hynds, S. Zaccaria, C. Swanton, N. McGranahan, and N. Kanu (2024). Replication timing alterations are associated with mutation acquisition during breast and lung cancer evolution. *Nature Communications* 15(1), 6039.
- Diggle, P. J. (2013). *Statistical Analysis of Spatial and Spatio-Temporal Point Patterns (3rd ed.)*. Chapman and Hall/CRC.
- Drummond, R. D., A. Defelicibus, M. Meyenberg, R. Valieris, E. Dias-Neto, R. A. Rosales, and I. T. da Silva (2023). Relating mutational signature exposures to clinical data in cancers via signeR 2.0. *BMC Bioinformatics* 24(1), 439.
- Dunson, D. B. and A. H. Herring (2005). Bayesian latent variable models for mixed discrete outcomes. *Biostatistics* 6(1), 11–25.

- Ernst, J. and M. Kellis (2017). Chromatin-state discovery and genome annotation with chromhmm. *Nature Protocols* 12(12), 2478–2492.
- Fischer, A., C. J. Illingworth, P. J. Campbell, and V. Mustonen (2013). EMu: probabilistic inference of mutational processes and their localization in the cancer genome. *Genome Biology* 14(4), R39.
- Gillis, N. (2020). *Nonnegative Matrix Factorization*.
- Grabski, I. N., L. Trippa, and G. Parmigiani (2025). Bayesian multi-study non-negative matrix factorization for mutational signatures. *Genome Biology* 26(1), 98.
- Gulhan, D. C., J. J.-K. Lee, G. E. M. Melloni, I. Cortés-Ciriano, and P. J. Park (2019). Detecting the mutational signature of homologous recombination deficiency in clinical samples. *Nature Genetics* 51(5), 912–919.
- Hansen, B., I. N. Grabski, G. Parmigiani, and R. D. Vito (2025). Bayesian probit multi-study non-negative matrix factorization for mutational signatures. arXiv:2502.01468 [stat.AP].
- Hansen, R. S., S. Thomas, R. Sandstrom, T. K. Canfield, R. E. Thurman, M. Weaver, M. O. Dorschner, S. M. Gartler, and J. A. Stamatoyannopoulos (2010). Sequencing newly replicated dna reveals widespread plasticity in human replication timing. *Proceedings of the National Academy of Sciences* 107(1), 139–144.
- Hodgkinson, A., Y. Chen, and A. Eyre-Walker (2012). The large-scale distribution of somatic mutations in cancer genomes. *Human Mutation* 33(1), 136–143.
- Hosseini, S. A., A. Khodadadi, K. Alizadeh, A. Arabzadeh, M. Farajtabar, H. Zha, and H. R. Rabiee (2020). Recurrent poisson factorization for temporal recommendation. *IEEE Transactions on Knowledge and Data Engineering* 32(1), 121–134.
- Islam, S. A., M. Díaz-Gay, Y. Wu, et al. (2022). Uncovering novel mutational signatures by de novo extraction with SigProfilerExtractor. *Cell Genomics* 2(11), 100179.
- Jaenisch, R. and A. Bird (2003). Epigenetic regulation of gene expression: how the genome integrates intrinsic and environmental signals. *Nature Genetics* 33(3), 245–254.
- Jin, H., D. C. Gulhan, B. Geiger, D. Ben-Isvy, D. Geng, V. Ljungström, and P. J. Park (2024). Accurate and sensitive mutational signature analysis with MuSiCal. *Nature Genetics* 56(3), 541–552.
- Joe, H. (2006). Generating random correlation matrices based on partial correlations. *Journal of Multivariate Analysis* 97(10), 2177–2189.
- Kang, B., E. M. Schliep, A. E. Gelfand, T. M. Yack, C. W. Clark, and R. S. Schick (2025). Analyzing whale calling through hawkes process modeling. *Journal of the American Statistical Association* 0(0), 1–13.
- Katainen, R., K. Dave, E. Pitkänen, et al. (2015). Ctf/cohesisin-binding sites are frequently mutated in cancer. *Nature Genetics* 47(7), 818–821.
- Kim, J., K. W. Mouw, P. Polak, et al. (2016). Somatic ERCC2 mutations are associated with a distinct genomic signature in urothelial tumors. *Nature Genetics* 48(6), 600–606.

- Kingman, J. F. C. (1993). *Poisson processes*, Volume 3 of *Oxford Studies in Probability*. New York: The Clarendon Press Oxford University Press. Oxford Science Publications.
- Koh, G., A. Degasperi, X. Zou, S. Momen, and S. Nik-Zainal (2021). Mutational signatures: emerging concepts, caveats and clinical applications. *Nature Reviews Cancer* 21(10), 619–637.
- Kucab, J. E., X. Zou, S. Morganello, M. Joel, A. S. Nanda, E. Nagy, C. Gomez, A. Degasperi, R. Harris, S. P. Jackson, V. M. Arlt, D. H. Phillips, and S. Nik-Zainal (2019). A compendium of mutational signatures of environmental agents. *Cell* 177(4), 821–836.e16.
- Landy, J. M., N. Basava, and G. Parmigiani (2025). bayesNMF: Fast Bayesian Poisson NMF with automatically learned rank applied to mutational signatures. arXiv:2502.18674.
- Landy, J. M., D. Zorzetto, R. D. Vito, and G. Parmigiani (2025). Causal inference for latent outcomes learned with factor models.
- Laursen, R., H. Chen, J. Demaray, K. Pelka, and B. E. Engelhardt (2025). Neighborhood nonnegative matrix factorization identifies patterns and spatially-variable genes in large-scale spatial transcriptomics data. *bioRxiv*.
- Lawless, J. F. (1987). Regression methods for Poisson process data. *Journal of the American Statistical Association* 82(399), 808–815.
- Lawrence, M., R. Gentleman, and V. Carey (2009, 05). rtracklayer: an R package for interfacing with genome browsers. *Bioinformatics* 25(14), 1841–1842.
- Lawrence, M., W. Huber, H. Pagès, P. Aboyoun, M. Carlson, R. Gentleman, M. T. Morgan, and V. J. Carey (2013, 08). Software for computing and annotating genomic ranges. *PLOS Computational Biology* 9(8), 1–10.
- Lawrence, M. S., P. Stojanov, P. Polak, et al. (2013). Mutational heterogeneity in cancer and the search for new cancer-associated genes. *Nature* 499(7457), 214–218.
- Lee, D. and H. S. Seung (2000). Algorithms for non-negative matrix factorization. In T. Leen, T. Dietterich, and V. Tresp (Eds.), *Advances in Neural Information Processing Systems*, Volume 13. MIT Press.
- Lee, D. D. and H. S. Seung (1999). Learning the parts of objects by non-negative matrix factorization. *Nature* 401(6755), 788–791.
- Lee, J., A. Lee, J.-K. Lee, J. Park, Y. Kwon, S. Park, H. Chun, Y. S. Ju, and D. Hong (2018, 05). Mutalisk: a web-based somatic mutation analysis toolkit for genomic, transcriptional and epigenomic signatures. *Nucleic Acids Research* 46(W1), W102–W108.
- Lee, S.-Y., H. Wang, H. J. Cho, R. Xi, and T.-M. Kim (2022). The shaping of cancer genomes with the regional impact of mutation processes. *Experimental & Molecular Medicine* 54(7), 1049–1060.

- Li, F., G. Mao, D. Tong, J. Huang, L. Gu, W. Yang, and G.-M. Li (2013). The histone mark H3K36me3 regulates human dna mismatch repair through its interaction with MutSalpha. *Cell* 153(3), 590–600.
- Li, S., F. W. Crawford, and M. B. Gerstein (2020). Using sigLASSO to optimize cancer mutation signatures jointly with sampling likelihood. *Nature Communications* 11(1), 3575.
- Lieberman-Aiden, E., N. L. van Berkum, L. Williams, M. Imakaev, T. Ragoczy, A. Telling, I. Amit, B. R. Lajoie, P. J. Sabo, M. O. Dorschner, R. Sandstrom, B. Bernstein, M. A. Bender, M. Groudine, A. Gnirke, J. Stamatoyannopoulos, L. A. Mirny, E. S. Lander, and J. Dekker (2009). Comprehensive mapping of long-range interactions reveals folding principles of the human genome. *Science* 326(5950), 289–293.
- Liu, M., Y. Wu, N. Jiang, A. Boot, and S. Rozen (2023, 01). msighdp: hierarchical dirichlet process mixture modeling for mutational signature discovery. *NAR Genomics and Bioinformatics* 5(1), lqad005.
- Lloyd, C., T. Gunter, M. Osborne, S. Roberts, and T. Nickson (2016, 09–11 May). Latent point process allocation. In A. Gretton and C. C. Robert (Eds.), *Proceedings of the 19th International Conference on Artificial Intelligence and Statistics*, Volume 51 of *Proceedings of Machine Learning Research*, Cadiz, Spain, pp. 389–397. PMLR.
- Loyfer, N., J. Magenheim, A. Peretz, et al. (2023). A DNA methylation atlas of normal human cell types. *Nature* 613(7943), 355–364.
- Makova, K. D. and R. C. Hardison (2015). The effects of chromatin organization on variation in mutation rates in the genome. *Nature Reviews Genetics* 16(4), 213–223.
- Martínez-Ruiz, C., J. R. M. Black, C. Puttick, et al. (2023). Genomic–transcriptomic evolution in lung cancer and metastasis. *Nature* 616(7957), 543–552.
- McCullagh, P. and J. Nelder (1989). *Generalized Linear Models, Second Edition*. Chapman and Hall/CRC Monographs on Statistics and Applied Probability Series. Chapman & Hall.
- Miller, A., L. Bornn, R. Adams, and K. Goldsberry (2014, 22–24 Jun). Factorized point process intensities: A spatial analysis of professional basketball. In E. P. Xing and T. Jebara (Eds.), *Proceedings of the 31st International Conference on Machine Learning*, Volume 32 of *Proceedings of Machine Learning Research*, Beijing, China, pp. 235–243. PMLR.
- Miller, J. W. and S. L. Carter (2020). Inference in generalized bilinear models. arXiv:2010.04896.
- Morganella, S., L. B. Alexandrov, D. Glodzik, et al. (2016). The topography of mutational processes in breast cancer genomes. *Nature Communications* 7(1), 11383.
- Murray, I., R. Adams, and D. MacKay (2010, 13–15 May). Elliptical slice sampling. In Y. W. Teh and M. Titterton (Eds.), *Proceedings of the Thirteenth International Conference on Artificial Intelligence and Statistics*, Volume 9 of *Proceedings of Machine Learning Research*, Chia Laguna Resort, Sardinia, Italy, pp. 541–548. PMLR.

- Nik-Zainal, S., L. B. Alexandrov, D. C. Wedge, et al. (2012). Mutational processes molding the genomes of 21 breast cancers. *Cell* 149(5), 979–993.
- Nik-Zainal, S., H. Davies, J. Staaf, et al. (2016). Landscape of somatic mutations in 560 breast cancer whole-genome sequences. *Nature* 534(7605), 47–54.
- Nishiyama, A. and M. Nakanishi (2021). Navigating the DNA methylation landscape of cancer. *Trends in Genetics* 37(11), 1012–1027.
- Otlu, B. and L. B. Alexandrov (2025). Evaluating topography of mutational signatures with sigprofilertopography. *Genome Biology* 26(1), 134.
- Otlu, B., M. Díaz-Gay, I. Vermes, E. N. Bergstrom, M. Zhivagui, M. Barnes, and L. B. Alexandrov (2023). Topography of mutational signatures in human cancer. *Cell Reports* 42(8), 112930.
- Pagès, H., P. Aboyoun, R. Gentleman, and S. DebRoy (2023). *Biostings: Efficient manipulation of biological strings*. R package version 2.68.1.
- Pancotti, C., C. Rollo, F. Codicè, G. Birolo, P. Fariselli, and T. Sanavia (2024). MUSE-XAE: MUtational Signature Extraction with eXplainable AutoEncoder enhances tumour types classification. *Bioinformatics* 40(5), btae320.
- Pandey, P., S. Arora, and G. L. Rosen (2022, April). MetaMutationalSigs: comparison of mutational signature refitting results made easy. *Bioinformatics (Oxford, England)* 38, 2344–2347.
- Pich, O., F. Muiños, R. Sabarinathan, I. Reyes-Salazar, A. Gonzalez-Perez, and N. Lopez-Bigas (2018). Somatic and germline mutation periodicity follow the orientation of the DNA minor groove around nucleosomes. *Cell* 175(4), 1074–1087.e18.
- Polak, P., R. Karlič, A. Koren, R. Thurman, R. Sandstrom, M. S. Lawrence, A. Reynolds, E. Rynes, K. Vlahoviček, J. A. Stamatoyannopoulos, and S. R. Sunyaev (2015). Cell-of-origin chromatin organization shapes the mutational landscape of cancer. *Nature* 518(7539), 360–364.
- Rosales, R. A., R. D. Drummond, R. Valieris, E. Dias-Neto, and I. T. da Silva (2016). signeR: an empirical Bayesian approach to mutational signature discovery. *Bioinformatics* 33(1), 8–16.
- Rousseau, J. and K. Mengersen (2011). Asymptotic behaviour of the posterior distribution in overfitted mixture models. *Journal of the Royal Statistical Society: Series B (Statistical Methodology)* 73(5), 689–710.
- Samur, M. K., A. Aktas Samur, M. Fulciniti, R. Szalat, T. Han, M. Shammas, P. Richardson, F. Magrangeas, S. Minvielle, J. Corre, et al. (2020). Genome-wide somatic alterations in multiple myeloma reveal a superior outcome group. *Journal of Clinical Oncology* 38(27), 3107–3118.
- Schmalohr, C. L. (2025). *Modeling the Tissue-Specific Somatic Mutation Rate Along the Genome Based on Genomic Features*. Ph. D. thesis, Universität zu Köln.

- Schuster-Böckler, B. and B. Lehner (2012). Chromatin organization is a major influence on regional mutation rates in human cancer cells. *Nature* 488(7412), 504–507.
- Shahrouzi, P., F. Forouz, A. Mathelier, V. N. Kristensen, and P. H. Duijf (2024). Copy number alterations: a catastrophic orchestration of the breast cancer genome. *Trends in Molecular Medicine* 30(8), 750–764.
- Sherman, M. A., A. U. Yaari, O. Priebe, F. Dietlein, P.-R. Loh, and B. Berger (2022). Genome-wide mapping of somatic mutation rates uncovers drivers of cancer. *Nature Biotechnology* 40(11), 1634–1643.
- Singh, V. K., A. Rastogi, X. Hu, Y. Wang, and S. De (2020). Mutational signature SBS8 predominantly arises due to late replication errors in cancer. *Communications Biology* 3(1), 421.
- Stamatoyannopoulos, J. A., I. Adzhubei, R. E. Thurman, G. V. Kryukov, S. M. Mirkin, and S. R. Sunyaev (2009). Human mutation rate associated with DNA replication timing. *Nature Genetics* 41(4), 393–395.
- Stratton, M. R., P. J. Campbell, and P. A. Futreal (2009). The cancer genome. *Nature* 458(7239), 719–724.
- Supek, F. and B. Lehner (2015). Differential DNA mismatch repair underlies mutation rate variation across the human genome. *Nature* 521(7550), 81–84.
- Supek, F. and B. Lehner (2017). Clustered mutation signatures reveal that error-prone DNA repair targets mutations to active genes. *Cell* 170(3), 534–547.e23.
- Supek, F. and B. Lehner (2019). Scales and mechanisms of somatic mutation rate variation across the human genome. *DNA Repair* 81, 102647. Cutting-edge Perspectives in Genomic Maintenance VI.
- Tate, J. G., S. Bamford, H. C. Jubb, et al. (2018, 10). COSMIC: the Catalogue Of Somatic Mutations In Cancer. *Nucleic Acids Research* 47(D1), D941–D947.
- Teh, Y. W., M. I. Jordan, M. J. Beal, and D. M. Blei (2006). Hierarchical Dirichlet processes. *Journal of the American Statistical Association* 101(476), 1566–1581.
- The ICGC/TCGA Pan-Cancer Analysis of Whole Genomes Consortium (2020). Pan-cancer analysis of whole genomes. *Nature* 578(7793), 82–93.
- Thurman, R. E., N. Day, W. S. Noble, and J. A. Stamatoyannopoulos (2007). Identification of higher-order functional domains in the human ENCODE regions. *Genome Research* 17(6), 917–927.
- Timmons, C., Q. Morris, and C. F. Harrigan (2022, 12). Regional mutational signature activities in cancer genomes. *PLOS Computational Biology* 18(12), 1–23.
- Tolstorukov, M. Y., N. Volfovsky, R. M. Stephens, and P. J. Park (2011). Impact of chromatin structure on sequence variability in the human genome. *Nature Structural & Molecular Biology* 18(4), 510–515.
- Townes, F. W. and B. E. Engelhardt (2023). Nonnegative spatial factorization applied to spatial genomics. *Nature Methods* 20(2), 229–238.

- Truccolo, W., U. T. Eden, M. R. Fellows, J. P. Donoghue, and E. N. Brown (2005). A point process framework for relating neural spiking activity to spiking history, neural ensemble, and extrinsic covariate effects. *Journal of Neurophysiology* 93(2), 1074–1089. PMID: 15356183.
- Vöhringer, H., A. V. Hoeck, E. Cuppen, and M. Gerstung (2021). Learning mutational signatures and their multidimensional genomic properties with tensorsignatures. *Nature Communications* 12(1), 3628.
- Wang, S., Z. Tao, T. Wu, and X.-S. Liu (2020). Sigflow: an automated and comprehensive pipeline for cancer genome mutational signature analysis. *Bioinformatics* 37(11), 1590–1592.
- Wang, Y., K. Woyshner, C. Sriworarat, G. Stein-O’Brien, L. A. Goff, and K. D. Hansen (2024). Multi-sample non-negative spatial factorization. *bioRxiv*.
- Wu, Y., E. H. Z. Chua, A. W. T. Ng, A. Boot, and S. G. Rozen (2022). Accuracy of mutational signature software on correlated signatures. *Scientific Reports* 12(1), 390.
- Xue, C., A. Zito, and J. W. Miller (2024). Improved control of Dirichlet location and scale near the boundary.
- Yost, K. E., Y. Zhao, K. L. Hung, et al. (2025). Three-dimensional genome landscape of primary human cancers. *Nature Genetics* 57(5), 1189–1200.
- Zhou, M. and L. Carin (2015). Negative binomial process count and mixture modeling. *IEEE Transactions on Pattern Analysis and Machine Intelligence* 37(2), 307–320.
- Zito, A. and J. W. Miller (2024). Compressive Bayesian non-negative matrix factorization for mutational signatures analysis. arXiv:2404.10974.

# SUPPLEMENTARY MATERIAL

## “Poisson process factorization for mutational signature analysis with genomic covariates”

Section S1 contains proofs for the statements in the main manuscripts. Section S2 presents a detailed derivation for the estimation algorithms. Section S3 reports additional simulation results. Section S4 presents additional plots and tables for the breast adenocarcinoma application.

### S1 PROOFS

**Proof of Proposition 1.** Under the assumptions of the statement, the likelihood we have that  $\int_0^T r_{ik}(t)\vartheta_{kj}(t)dt = \int_0^1 r_{ik}\theta_{kj}dt = r_{ik}\theta_{kj}$ . Then, the likelihood can be written as

$$\begin{aligned} \mathcal{L}(\{N_{ij}; t_1, \dots, t_{N_{ij}}\}_{ij}) &= \prod_{ij} \exp \left\{ - \sum_{k=1}^K r_{ik}\theta_{kj} \right\} \prod_{n=1}^{N_{ij}} \sum_{k=1}^K r_{ik}\theta_{kj} \\ &= \exp \left\{ - \sum_j \sum_{k=1}^K \theta_{kj} \right\} \left( \sum_{k=1}^K r_{ik}\theta_{kj} \right)^{N_{ij}}. \end{aligned}$$

This is proportional to the likelihood from the Poisson model in Equation (1), in terms of  $r_{ik}$  and  $\theta_{kj}$ . □

**Proof of Proposition 2.** The result follows from the superposition theorem of Poisson processes. See Theorem 3.3 in [Last and Penrose \(2017\)](#). □

### S2 DERIVATIONS OF THE ALGORITHMS

#### S2.1 MAXIMUM A POSTERIORI

We present a detailed derivation of the majorization-minimization strategy used to obtain Algorithm 1. By plugging Equation (5) and Equation (2) into Equation (2) and taking the product across pairs  $i, j$ , we have

$$\begin{aligned} -\log \pi(R, \Theta, B, \mu, \sigma^2 \mid \{t_1, \dots, t_{N_{ij}}\}_{ij}) &= \\ &= \sum_{jk} \theta_{kj} \int_0^T \frac{1}{2} c_j(t) e^{\beta_k^\top \mathbf{x}(t)} dt - \sum_{ij} \sum_{n=1}^{N_{ij}} \log \left( \sum_{k=1}^K r_{ik}\theta_{kj} \frac{1}{2} c_j(t_n) e^{\beta_k^\top \mathbf{x}(t_n)} \right) \quad (\text{Log-likelihood}) \\ &\quad - \sum_{ik} (\alpha_{ik} - 1) \log r_{ik} \quad (\text{Signatures}) \\ &\quad - \sum_{kj} -a \log \mu_k + (a - 1) \log \theta_{kj} - \theta_{kj} \frac{a}{\mu_k} \int_0^T \frac{1}{2} c_j(t) dt \quad (\text{Baseline activities}) \quad (\text{S1}) \\ &\quad - \sum_k -\frac{p}{2} \log \sigma_k^2 - \frac{1}{2\sigma_k^2} \beta_k^\top \beta_k \quad (\text{Regression coefficients}) \\ &\quad - \sum_k -(a_0 + 1) \log \mu_k - \frac{b_0}{\mu_k} \quad (\text{Relevance weights}) \\ &\quad - \sum_k -(c_0 + 1) \log \sigma_k^2 - \frac{d_0}{\sigma_k^2} \quad (\text{Variances}) \end{aligned}$$

subject to  $\sum_{i=1}^I r_{ik} = 1$  for each  $k = 1, \dots, K$ . For generality, we consider the case when  $\mu_k \sim \text{InvGa}(a_0, b_0)$ . Equation (S1). The compressive hyperprior in Equation (8) is recovered by letting  $a_0 = aJ + 1$  and  $b_0 = \varepsilon aJ$ . We first re-state the following useful property for the logarithm of a sum.

**Lemma 1.** *For any  $\eta_1, \dots, \eta_K$  with  $\eta_k \geq 0$  and  $\sum_{k=1}^K \eta_k = 1$ , it holds that*

$$-\log \sum_{k=1}^K x_k \leq -\sum_{k=1}^K \eta_k \log \frac{x_k}{\eta_k}.$$

We will derive all the steps using the result in Lemma 1.

### Derivation of Step 1 - mutational signatures

The update for  $r_k = (r_{1k}, \dots, r_{Ik})$  is obtained by solving the following problem jointly for each  $r_{ik}$ :

$$\begin{aligned} \arg \min_{r_{ik} \geq 0} f_r(r_{ik}) = & \sum_{jk} \theta_{kj} \int_0^T \frac{1}{2} c_j(t) e^{\beta_k^\top \mathbf{x}(t)} dt - \sum_j \sum_{n=1}^{N_{ij}} \log \left( \sum_{k=1}^K r_{ik} \theta_{kj} \frac{1}{2} c_j(t_n) e^{\beta_k^\top \mathbf{x}(t_n)} \right) \\ & - (\alpha_{ik} - 1) \log r_{ik} + \tau \left( 1 - r_{ik} - \sum_{s \neq k} r_{is} \right) \end{aligned}$$

where  $\tau$  is the Lagrange multiplier for the constraint  $\sum_{i=1}^I r_{ik} = 1$ . In Lemma 1, our candidate weights are  $\eta_k = \tilde{r}_{ik} \theta_{kj} e^{\beta_k^\top \mathbf{x}(t_n)} / \sum_s \tilde{r}_{is} \theta_{sj} e^{\beta_s^\top \mathbf{x}(t_n)}$  for some  $\tilde{r}_{ik}$ . Then, a majorizer of  $f(r_{ik})$  is the function  $g(\tilde{r}_{ik}, r_{ik})$  defined as

$$\begin{aligned} g_r(\tilde{r}_{ik}, r_{ik}) = & \sum_{jk} \theta_{kj} \int_A \frac{1}{2} c_j(t) e^{\beta_k^\top \mathbf{x}(t)} dt - \sum_{jk} \sum_{n=1}^{N_{ij}} \frac{\tilde{r}_{ik} \theta_{kj} e^{\beta_k^\top \mathbf{x}(t_n)}}{\sum_s \tilde{r}_{is} \theta_{sj} e^{\beta_s^\top \mathbf{x}(t_n)}} \log \left\{ \frac{\sum_s \tilde{r}_{is} \theta_{sj} e^{\beta_s^\top \mathbf{x}(t_n)}}{\tilde{r}_{ik} \theta_{kj} e^{\beta_k^\top \mathbf{x}(t_n)}} r_{ik} \theta_{kj} \frac{1}{2} c_j(t_n) e^{\beta_k^\top \mathbf{x}(t_n)} \right\} \\ & - (\alpha_{ik} - 1) \log r_{ik} + \tau \left( 1 - r_{ik} - \sum_{s \neq k} r_{is} \right) \end{aligned} \tag{S2}$$

Taking the derivative of Equation (S2) with respect to  $r_{ik}$  and setting them to zero yields the equation

$$\frac{\partial g_r(\tilde{r}_{ik}, r_{ik})}{\partial r_{ik}} = 0 \iff -\frac{1}{r_{ik}} \sum_j \sum_{n=1}^{N_{ij}} \frac{\tilde{r}_{ik} \theta_{kj} e^{\beta_k^\top \mathbf{x}(t_n)}}{\sum_s \tilde{r}_{is} \theta_{sj} e^{\beta_s^\top \mathbf{x}(t_n)}} - \frac{\alpha_{ik} - 1}{r_{ik}} + \tau = 0,$$

which implies that

$$r_{ik} = \frac{1}{\tau} \left( \alpha_{ik} - 1 + \tilde{r}_{ik} \frac{\theta_{kj} e^{\beta_k^\top \mathbf{x}(t_n)}}{\sum_s \tilde{r}_{is} \theta_{sj} e^{\beta_s^\top \mathbf{x}(t_n)}} \right)$$

Finally, taking the derivative with respect to the Lagrange multiplier leads to  $\sum_{i=1}^I r_{ik} = 1$ . Plugging in this condition and solving for  $\tau$  yields the desired update.

### Derivation of Step 2 — Baseline activity

We optimize over  $\theta_{kj} \geq 0$  keeping all other parameters fixed. In particular, the minimization problem is

$$\begin{aligned} \arg \min_{\theta_{kj} \geq 0} f_{\theta}(\theta_{kj}) &= \theta_{kj} \int_0^T \frac{1}{2} c_j(t) e^{\beta_k^{\top} \mathbf{x}(t)} dt - \sum_i \sum_{n=1}^{N_{ij}} \log \left( \sum_{k=1}^K r_{ik} \theta_{kj} \frac{1}{2} c_j(t_n) e^{\beta_k^{\top} \mathbf{x}(t_n)} \right) \\ &\quad + (a-1) \log \theta_{kj} + \theta_{kj} \frac{a}{\mu_k} \int_0^T \frac{1}{2} c_j(t) dt \end{aligned}$$

Using the same majorization trick as in Step 1 with  $\eta_k = r_{ik} \tilde{\theta}_{kj} e^{\beta_k^{\top} \mathbf{x}(t_n)} / \sum_s r_{is} \tilde{\theta}_{sj} e^{\beta_s^{\top} \mathbf{x}(t_n)}$  one obtains

$$\begin{aligned} g_{\theta}(\tilde{\theta}_{kj}, \theta_{kj}) &= \\ \theta_{kj} \int_0^T \frac{1}{2} c_j(t) e^{\beta_k^{\top} \mathbf{x}(t)} dt &- \sum_{n=1}^{N_{ij}} \frac{r_{ik} \tilde{\theta}_{kj} e^{\beta_k^{\top} \mathbf{x}(t_n)}}{\sum_s r_{is} \tilde{\theta}_{sj} e^{\beta_s^{\top} \mathbf{x}(t_n)}} \log \left\{ \frac{\sum_s r_{is} \tilde{\theta}_{sj} e^{\beta_s^{\top} \mathbf{x}(t_n)}}{r_{ik} \tilde{\theta}_{kj} e^{\beta_k^{\top} \mathbf{x}(t_n)}} r_{ik} \theta_{kj} \frac{1}{2} c_j(t_n) e^{\beta_k^{\top} \mathbf{x}(t_n)} \right\} \quad (\text{S3}) \\ &\quad + (a-1) \log \theta_{kj} + \theta_{kj} \frac{a}{\mu_k} \int_0^T \frac{1}{2} c_j(t) dt. \end{aligned}$$

Taking the derivative of Equation (S3) with respect to  $\theta_{kj}$  and setting it to zero yields

$$\frac{\partial g_{\theta}(\tilde{\theta}_{kj}, \theta_{kj})}{\partial \theta_{kj}} = \int_0^T \frac{1}{2} c_j(t) e^{\beta_k^{\top} \mathbf{x}(t)} dt + \frac{a}{\mu_k} \int_0^T \frac{1}{2} c_j(t) dt - \frac{1}{\theta_{kj}} \sum_i \sum_{n=1}^{N_{ij}} \frac{r_{ik} \tilde{\theta}_{kj} e^{\beta_k^{\top} \mathbf{x}(t_n)}}{\sum_s r_{is} \tilde{\theta}_{sj} e^{\beta_s^{\top} \mathbf{x}(t_n)}} - \frac{a-1}{\theta_{kj}} = 0,$$

leading to the update

$$\theta_{kj} = a - 1 + \tilde{\theta}_{kj} \times \frac{\mu_k}{a \int_0^T \frac{1}{2} c_j(t) dt + \mu_k \int_0^T \frac{1}{2} c_j(t) e^{\beta_k^{\top} \mathbf{x}(t)} dt} \sum_i \sum_{n=1}^{N_{ij}} \frac{r_{ik} e^{\beta_k^{\top} \mathbf{x}(t_n)}}{\sum_s r_{is} \tilde{\theta}_{sj} e^{\beta_s^{\top} \mathbf{x}(t_n)}}.$$

Note that in this case there is need to further use any Lagrange multiplier since the above update is guaranteed to keep  $\theta_{kj}$  non-negative as long as  $a \geq 1$ . If instead  $a \in (0, 1)$ , non-negativity is not guaranteed.

### Derivation of Step 3 — Regression coefficients

Here we optimize with respect to  $\beta_k$  (for fixed  $R, \Theta, \dots$ ):

$$\arg \min_{\beta_k} q(\beta_k) = \sum_j \theta_{kj} \int_0^T \frac{1}{2} c_j(t) e^{\beta_k^{\top} \mathbf{x}(t)} dt - \sum_{ij} \sum_{n=1}^{N_{ij}} \log \left( \sum_s r_{is} \theta_{sj} \frac{1}{2} c_j(t_n) e^{\beta_s^{\top} \mathbf{x}(t_n)} \right) + \frac{1}{2\sigma_k^2} \beta_k^{\top} \beta_k$$

We apply the log-sum majorization as above, then do a local second-order (quadratic) approximation to  $q(\beta_k)$ .

The gradient and Hessian are

$$\begin{aligned} \mathbf{g}_k &= - \sum_j \theta_{kj} \int \frac{1}{2} c_j(t) e^{\beta_k^{\top} \mathbf{x}(t)} \mathbf{x}(t) dt + \sum_{ij} \sum_{n=1}^{N_{ij}} w_{ij}^{(k)}(t_n) \mathbf{x}(t_n) - \frac{1}{\sigma_k^2} \beta_k \\ \mathbf{H}_k &= - \sum_j \theta_{kj} \int \frac{1}{2} c_j(t) e^{\beta_k^{\top} \mathbf{x}(t)} \mathbf{x}(t) \mathbf{x}(t)^{\top} dt - \frac{1}{\sigma_k^2} I_p \end{aligned}$$

where  $w_{ij}^{(k)}(t_n) = (r_{ik}\theta_{kj}e^{\beta_k^\top \mathbf{x}(t_n)})/(\sum_{s=1}^K r_{is}\theta_{sj}e^{\beta_s^\top \mathbf{x}(t_n)})$  is the weight for signature  $k$  at location  $t_n$  as determined by the majorization. We update  $\beta_k \leftarrow \beta_k - \mathbf{H}_k^{-1} \mathbf{g}_k$ , using the correction proposed by [Miller and Carter \(2020\)](#); see Section 3.1.

#### Derivation of Step 4 — Relevance weights and variance parameters

The updates for  $\mu_k$  and  $\sigma_k^2$  follow from maximizing the log-posterior, and are available analytically.

$$\mu_k = \frac{a \sum_j \theta_{kj} \int_0^T \frac{1}{2} c_j(t) dt + b_0}{aJ + a_0 + 1}, \quad \sigma_k^2 = \frac{d_0 + \sum_{\ell=1}^p \beta_{pk}^2 / 2}{c_0 + p/2 + 1}.$$

## S2.2 MARKOV CHAIN MONTE CARLO

The likelihood function is written as

$$\mathcal{L}(\{t_1, \dots, t_{N_{ij}}\}_{ij}) = \exp \left\{ - \sum_{jk} \int_0^T \frac{1}{2} c_j(t) \theta_{kj} e^{\beta_k^\top \mathbf{x}(t)} dt \right\} \prod_{ij} \prod_{n=1}^{N_{ij}} \left( \sum_{k=1}^K \frac{1}{2} c_j(t_n) r_{ik} \theta_{kj} e^{\beta_k^\top \mathbf{x}(t_n)} \right)$$

We adopt a data augmentation approach typical of Poisson factorization ([Dunson and Herring, 2005](#)). In particular, introducing one multinomial random variable for each of the detected mutations so that

$$W_{ij}(t_n) = (W_{ij1}(t_n), \dots, W_{ijK}(t_n)) \sim \text{Multinomial} \{1; p_{ij1}(t_n), \dots, p_{ijK}(t_n)\},$$

and where

$$p_{ijk}(t_n) = \mathbb{P}(W_{ijk}(t_n) = 1 \mid R, \Theta, B) = \frac{r_{ik} \theta_{kj} e^{\beta_k^\top \mathbf{x}(t_n)}}{\sum_{s=1}^K r_{is} \theta_{sj} e^{\beta_s^\top \mathbf{x}(t_n)}},$$

then one can write the full posterior as follows.

$$\begin{aligned} \pi(R, \Theta, B, \mu, \sigma^2, W \mid \{t_1, \dots, t_{N_{ij}}\}_{ij}) &\propto \\ &\propto \exp \left\{ - \sum_{jk} \int_0^T \frac{1}{2} c_j(t) \theta_{kj} e^{\beta_k^\top \mathbf{x}(t)} dt \right\} \prod_{ij} \prod_{n=1}^{N_{ij}} \prod_{k=1}^K \left( \frac{1}{2} c_j(t_n) r_{ik} \theta_{kj} e^{\beta_k^\top \mathbf{x}(t_n)} \right)^{W_{ijk}(t_n)} && \text{(Likelihood)} \\ &\times \prod_{k=1}^K \prod_i r_{ik}^{\alpha_{ik}-1} && \text{(Signatures)} \\ &\times \prod_{k=1}^K \prod_j \mu_k^{-a} \theta_{kj}^{a-1} \exp \left\{ - \theta_{kj} \frac{a}{\mu_k} \int_0^T \frac{1}{2} c_j(t) dt \right\} && \text{(Baseline)} \\ &\times \prod_{k=1}^K (\sigma_k^2)^{-p/2} \exp \left\{ - \frac{1}{2\sigma_k^2} \beta_k^\top \beta_k \right\} && \text{(Reg. coef.)} \\ &\times \prod_{k=1}^K \log \mu_k^{-a_0-1} \exp \{-b_0/\mu_k\} && \text{(Rel. weights)} \\ &\times \prod_{k=1}^K (\sigma_k^2)^{-c_0-1} \exp \{-d_0/\sigma_k^2\} && \text{(Variances)} \end{aligned} \tag{S4}$$

All the full conditionals in Algorithm 2 follow from standard conjugate updates from Equation (S4).

### S2.3 MAP FOR THE BASELINE COMPRESSIVE NMF

The CompNMF model of Zito and Miller (2024) is a special case of the PPF model where  $\beta_k = 1$  for all signatures, and  $\vartheta_{kj}(t) = \theta_{kj}/T$  for all  $t$ . Hence, the maximum a posteriori can be derived with the same rules described in Section 3.1. Notice that these rules are valid if  $a \geq 1$  and  $\alpha_{ik} \geq 1$ .

The algorithm below reports the majorization-minimization rules for the baseline NMF case with automatic selection for the number of factors. Unlike the PPF, these updates can be written using matrix multiplication rules, which are particularly fast. We stop the algorithm when two successive iterations of the log-posterior have a relative difference below  $10^{-7}$ .

---

**Algorithm S1.** MAP updates for Compressive NMF

---

1 **Signature mixtures** – Update the signature matrix  $R$  as:

$$R \leftarrow \text{normalize} \left\{ (A - 1) + R \circ \left( \frac{X}{R\Theta} \Theta^\top \right) \right\}$$

where  $A \in \mathbb{R}^{I \times K}$  is a prior matrix where the  $k$ th column is given by  $\alpha_{1k}, \dots, \alpha_{Ik}$ ,  $\circ$  denotes element-wise multiplication,  $\frac{X}{R\Theta}$  is element-wise division, and  $\text{normalize}\{\cdot\}$  makes each column of  $R$  sum to one.

2 **Signature weights** – Let  $\mu = (\mu_1, \dots, \mu_K)$  be the relevance weight vector. Extend  $\mu$  into a  $K \times M$  matrix by repeating it across columns, denoted  $\mu_{\text{all}}$ . Update the signature weight matrix  $\Theta$  as:

$$\Theta \leftarrow \frac{\mu_{\text{all}}}{a + \mu_{\text{all}}} \circ \left[ a - 1 + \Theta \circ \left( R^\top \frac{X}{R\Theta} \right) \right].$$

3 **Relevance weights** – Update each relevance weight  $\mu_k$  as:

$$\mu_k \leftarrow \frac{a \sum_{j=1}^J \theta_{kj} + b_0}{aJ + a_0 + 1}$$

**Output:** Updated  $R$ ,  $\Theta$ ,  $\mu$ .

---

### S3 ADDITIONAL SIMULATION RESULTS

We now present an extended version of the simulation results in Section 4, using the following models.

- {0} MAP, true – the MAP for the correctly specified model with  $c_j(t)$  set to the true values and  $p = p_{\text{true}} = 5$ .
- {1} MAP, CompNMF – the MAP of the model in Equation (1) with priors as in [Zito and Miller \(2024\)](#).
- {2} Copies, no  $\mathbf{x}$  – the MAP of the model with  $c_j(t)$  set to the true values, but excluding the covariates.
- {3} MAP, all  $\mathbf{x}$  – the MAP for the model with all  $p = 10$  covariates and the true values for  $c_j(t)$ .
- {4} MCMC, all  $\mathbf{x}$  – the posterior mean for model (3) calculated by starting Algorithm 2 from the MAP.
- {5} MCMC, all  $\mathbf{x}$ ,  $\Delta_b = 200$  – the posterior mean for model (v) where covariates are aggregated by further averaging their values into consecutive groups of 2.
- {6} MCMC, all  $\mathbf{x}$ ,  $\Delta_b = 500$ . The same as above, but with consecutive groups of 5 bins.

Our goal is again to test the performance of different versions of our methods. Specifically, we run models {5} and {6} to test the effect of approximating the integral in Equation (11) using a coarser grid compared to the true data generating process. While these approximations are useful to save memory and computational time, we aim at testing whether they hurt estimation performance.

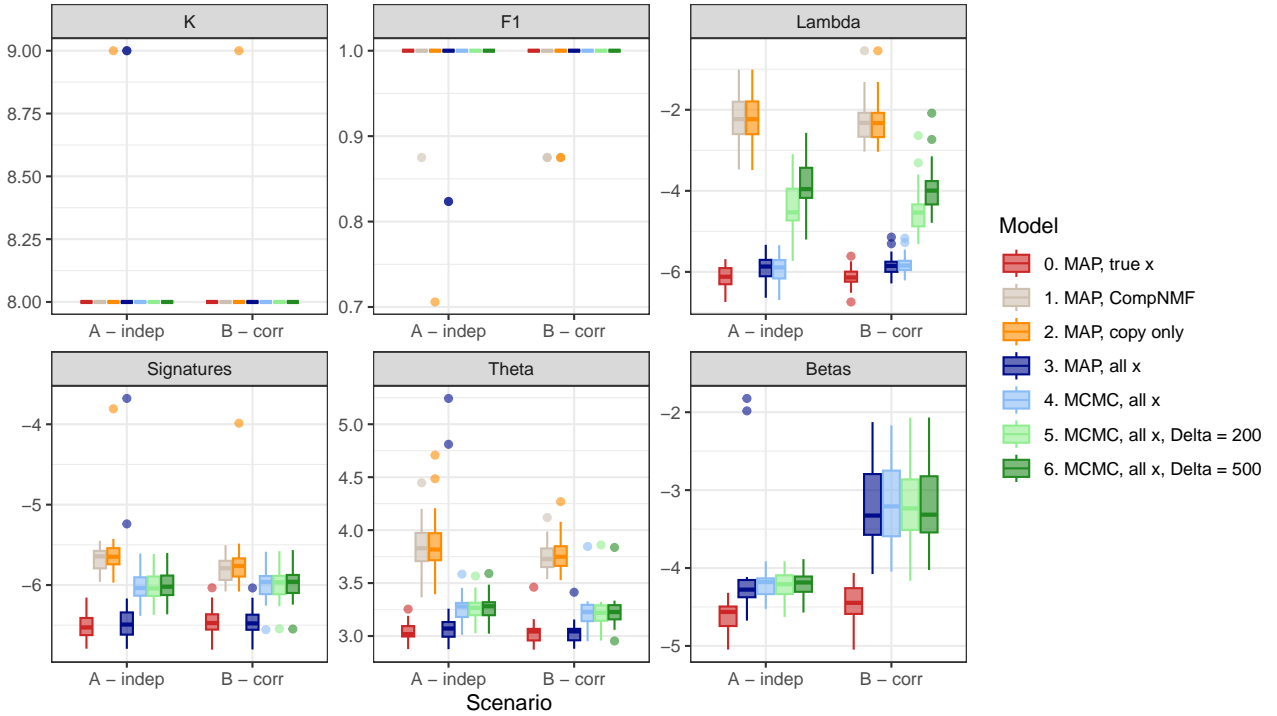


Figure S1: Extended simulation results. Panel  $K$  denotes the inferred number of signatures in the 20 replicates. Panel  $F1$  indicates the  $F_1$  score. The remaining plots report the logRMSE as in Figure 2.

We again set  $a = 1.01$ ,  $\alpha_{ik} = 1.01$ ,  $\varepsilon = 0.001$ ,  $K = 15$ , and  $c_0 = 100$ ,  $d_0 = 1$ . Figure S1 reports the results of the simulation for both Scenarios. On top of the quantities displayed in Figure 2, we also add one panel reporting the estimated number of signatures in the replicates, and a panel reporting the  $F_1$  score for each simulation. This last metric is obtained as  $F_1 = 2 \times \text{precision} \times \text{sensitivity} / (\text{precision} + \text{sensitivity})$ , where *precision* as the proportion of estimated signatures that have a cosine similarity  $\geq 0.9$  with at least one of

the ground truth signatures, and *sensitivity* is the proportion of ground truth signatures for which there is an estimated signature with cosine similarity  $\geq 0.9$ ; refer to Islam et al. (2022). Hence, the  $F_1$  is a measure of how similar  $\hat{R}$  and  $R_0$  are, with values close to 1 indicating very high agreement. The other panels display again the log RMSE with respect to the true quantities, where the logarithm is taken to aid visualization.

We notice the following facts. First, interestingly, all models have very high accuracy with respect to the true number of factors ( $K = 8$ ), and a perfect  $F_1$  score with only a few exceptions. Hence, we can trust all models to correctly retrieve the signatures in the data. Second, estimates for the model parameters are rarely affected by the presence of copy numbers compared to the constant NMF case. This is likely due to the limited impact of the additional copies on the generated data. Third, we do not detect a strong difference between the estimates for  $R_0$ ,  $\Theta_0([0, T])$ , and  $B$  by running models {4} versus {5} and {6}. This suggests that approximating the integral in the intensity function using coarser partitions does not impact the coefficients. Instead, differences are detected when estimating the total intensity  $\Lambda$  compared to the truth.

We further benchmark the performance in terms of times and number of iterations to obtain the MAP in each model in Table S1. We see that the longest run is given by the model with all the covariates, while the MAP for CompNMF obtained in Algorithm S1 is sizably faster than the other ones when considering the elapsed times, though convergence requires much more iterations.

Table S1: Computation time and number of iterations for MAP-based methods. Numbers indicate averages across 20 randomly generated datasets, with standard deviation in parentheses beneath each entry.

| MODEL SETTING  | SCENARIO A       |                      | SCENARIO B       |                      |
|----------------|------------------|----------------------|------------------|----------------------|
|                | TIME (MIN)       | ITERATIONS           | TIME (MIN)       | ITERATIONS           |
| MAP, TRUE      | 23.42<br>(11.62) | 384.50<br>(142.44)   | 23.33<br>(19.87) | 430.50<br>(271.18)   |
| MAP, COMPNMF   | 0.009<br>(0.007) | 4641.85<br>(1895.65) | 0.009<br>(0.005) | 3694.85<br>(1288.91) |
| MAP, COPY ONLY | 8.71<br>(6.26)   | 626.00<br>(272.69)   | 7.65<br>(5.32)   | 581.00<br>(258.27)   |
| MAP, ALL       | 26.81<br>(17.77) | 373.00<br>(195.41)   | 19.83<br>(10.48) | 343.50<br>(271.07)   |

We conclude by reporting the effective sample sizes for  $R$ ,  $\Theta$ ,  $B$ ,  $\mu$ ,  $\sigma^2$  and the log-posterior for models {4}, {5} and {6}. Results are obtained by running using the last 1500 samples (except timing, which considers the total 3000 iterations). The main impact simulation Scenarios is seen in the effective sample size of the regression coefficients  $\beta_k$ , which becomes in Scenario B compared to A. Other quantities do not suffer in the same manner.

Table S2: Average computation time and effective sample sizes (ESS) in the simulation section. Numbers indicate averages across 20 datasets; standard deviation is in parentheses below the mean. ESS are calculated over 1500 samples.

| SETTING          | TIME (MIN)        |                   | ESS $B$         |                 | ESS $R$           |                   | ESS $\Theta$      |                   | ESS $\mu$           |                     | ESS $\sigma^2$     |                     | ESS logPost       |                    |
|------------------|-------------------|-------------------|-----------------|-----------------|-------------------|-------------------|-------------------|-------------------|---------------------|---------------------|--------------------|---------------------|-------------------|--------------------|
|                  | A                 | B                 | A               | B               | A                 | B                 | A                 | B                 | A                   | B                   | A                  | B                   | A                 | B                  |
| $\Delta_b = 100$ | 131.59<br>(28.84) | 137.03<br>(31.63) | 49.32<br>(2.17) | 18.96<br>(3.07) | 387.94<br>(43.39) | 388.73<br>(35.58) | 438.75<br>(40.85) | 453.74<br>(39.46) | 1171.81<br>(127.70) | 1205.99<br>(123.45) | 1433.16<br>(56.89) | 1311.81<br>(102.60) | 467.21<br>(62.05) | 474.47<br>(77.76)  |
| $\Delta_b = 200$ | 141.73<br>(18.38) | 141.26<br>(18.53) | 49.48<br>(2.22) | 18.80<br>(3.69) | 388.49<br>(42.04) | 388.63<br>(36.32) | 444.08<br>(36.86) | 452.52<br>(38.24) | 1166.61<br>(102.73) | 1215.65<br>(94.38)  | 1463.02<br>(56.65) | 1333.83<br>(76.93)  | 484.76<br>(97.16) | 491.23<br>(61.86)  |
| $\Delta_b = 500$ | 91.76<br>(18.18)  | 93.02<br>(26.63)  | 48.37<br>(1.97) | 18.99<br>(2.95) | 385.08<br>(42.25) | 385.91<br>(35.36) | 441.23<br>(38.33) | 454.72<br>(38.47) | 1181.76<br>(109.40) | 1217.78<br>(118.11) | 1451.47<br>(59.68) | 1294.16<br>(112.36) | 489.12<br>(68.30) | 463.25<br>(104.74) |

## S4 ADDITIONAL DETAILS ON BREAST CANCER APPLICATION

Table S3: Summary of selected ENCODE and GEO datasets with .bigWig accession file types.

| Repository | Covariate            | Measurement              | Type         | File  |
|------------|----------------------|--------------------------|--------------|---|
| ENCODE     | CTCF                 | Fold change over control | Primary cell | ENCFF101RHP.bigWig                                    |
| ENCODE     | H3K27ac              | Fold change over control | Primary cell | ENCFF981WTU.bigWig                                    |
| ENCODE     | H3K27me3             | Fold change over control | Primary cell | ENCFF322JKF.bigWig                                    |
| ENCODE     | H3K36me3             | Fold change over control | Primary cell | ENCFF175PNA.bigWig                                    |
| ENCODE     | H3K4me1              | Fold change over control | Primary cell | ENCFF531OEA.bigWig                                    |
| ENCODE     | H3K4me3              | Fold change over control | Primary cell | ENCFF094MQS.bigWig                                    |
| ENCODE     | H3K4me3              | Fold change over control | Primary cell | ENCFF240TPL.bigWig                                    |
| ENCODE     | H3K4me3              | Fold change over control | Primary cell | ENCFF925FUX.bigWig                                    |
| ENCODE     | H3K9me3              | Fold change over control | Primary cell | ENCFF709GNN.bigWig                                    |
| ENCODE     | CTCF                 | Fold change over control | Tissue       | ENCFF143AFG.bigWig                                    |
| ENCODE     | CTCF                 | Fold change over control | Tissue       | ENCFF663JVM.bigWig                                    |
| ENCODE     | H3K27ac              | Fold change over control | Tissue       | ENCFF984VUL.bigWig                                    |
| ENCODE     | H3K27me3             | Fold change over control | Tissue       | ENCFF353WUO.bigWig                                    |
| ENCODE     | H3K36me3             | Fold change over control | Tissue       | ENCFF529OVO.bigWig                                    |
| ENCODE     | H3K4me1              | Fold change over control | Tissue       | ENCFF467DBD.bigWig                                    |
| ENCODE     | H3K4me3              | Fold change over control | Tissue       | ENCFF216DKX.bigWig                                    |
| ENCODE     | H3K9me3              | Fold change over control | Tissue       | ENCFF764JHZ.bigWig                                    |
| ENCODE     | Nucleosome occupancy | Signal                   | K562         | GSM920557_hg19_wgEncodeSydhNsomeK562Sig.bigWig        |
| ENCODE     | Replication timing   | Wavelet-smoothed signal  | MCF7         | wgEncodeUwRepliSeqMcf7WaveSignalRep1.bigWig           |
| BSgenome   | GC content           | Percent                  | hg19         | BSgenome.Hsapiens.UCSC.hg19                           |
| GEO        | Methylation          | Beta score               |              | GSM5652347_Breast-Luminal-Epithelial-Z000000V2.bigwig |
| GEO        | Methylation          | Beta score               |              | GSM5652348_Breast-Luminal-Epithelial-Z000000VJ.bigwig |
| GEO        | Methylation          | Beta score               |              | GSM5652349_Breast-Luminal-Epithelial-Z000000VN.bigwig |
| GEO        | Methylation          | Beta score               |              | GSM5652350_Breast-Basal-Epithelial-Z000000V6.bigwig   |
| GEO        | Methylation          | Beta score               |              | GSM5652351_Breast-Basal-Epithelial-Z000000VG.bigwig   |
| GEO        | Methylation          | Beta score               |              | GSM5652352_Breast-Basal-Epithelial-Z000000VL.bigwig   |
| GEO        | Methylation          | Beta score               |              | GSM5652353_Breast-Basal-Epithelial-Z0000043E.bigwig   |

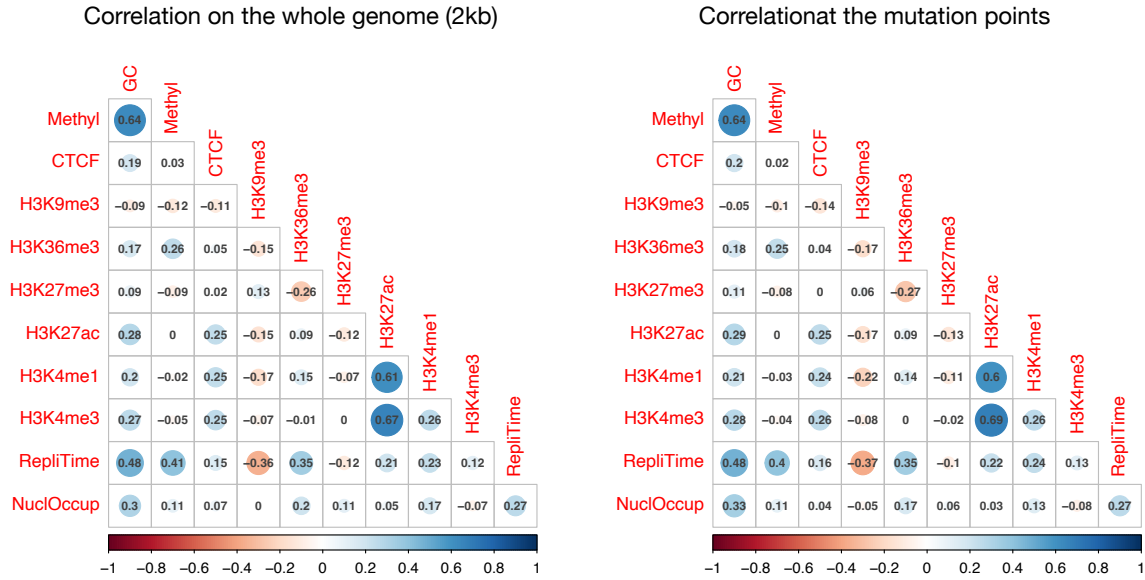


Figure S2: Correlation between genomic covariates at the 2kb resolution. Left: correlations over the whole genome. Right: correlation of the values at the mutation points. Regions that have  $\Delta_b = 0$  have been excluded to compute the values.

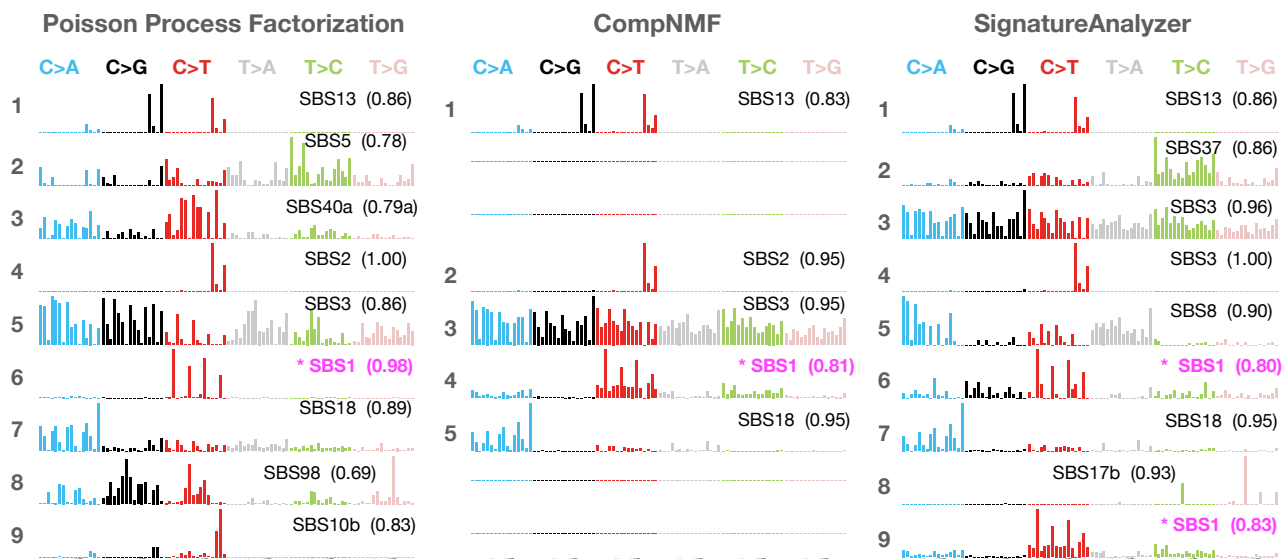


Figure S3: Estimated signatures in ICGC breast adenocarcinoma. Left: result of the Poisson process factorization. Center: results of the CompNMF, Algorithm S1. Right: output from SIGNATUREANALYZER.

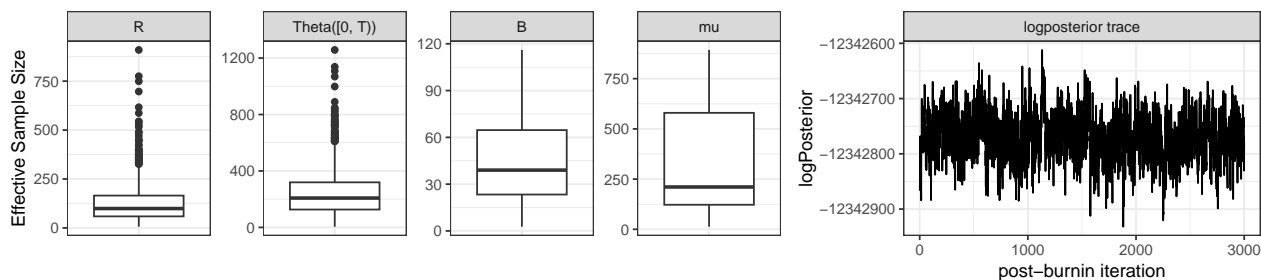


Figure S4: Left: effective sample sizes for model parameters in the *de novo* analysis. Right: traceplot for the logposterior. Values are computed over 3,000 iterations.

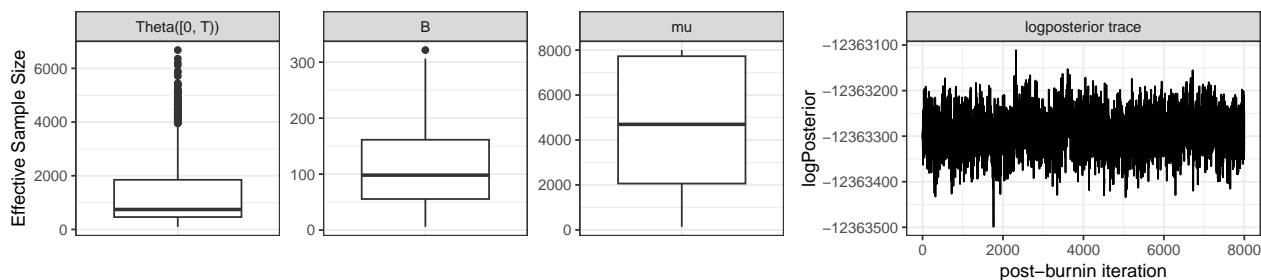


Figure S5: Left: effective sample sizes for model parameters in the fixed-signatures analysis. Right: traceplot for the logposterior. Values are computed over 8,000 iterations.

## REFERENCES

Islam, S. A., M. Díaz-Gay, Y. Wu, et al. (2022). Uncovering novel mutational signatures by *de novo* extraction with SigProfilerExtractor. *Cell Genomics* 2(11), 100179.

Last, G. and M. Penrose (2017). *Lectures on the Poisson Process*. Institute of Mathematical Statistics Textbooks. Cambridge University Press.

Miller, J. W. and S. L. Carter (2020). Inference in generalized bilinear models. arXiv:2010.04896.

Zito, A. and J. W. Miller (2024). Compressive Bayesian non-negative matrix factorization for mutational signatures analysis. arXiv:2404.10974.